Università degli Studi di Napoli
Federico II

Graduate School of Physical Sciences
PhD course in Fundamental and Applied Physics

Doctoral dissertation by
Roberta Caruso

Properties of unconventional S-F-S Josephson junctions

Supervisor
Prof. Francesco Tafuri

Coordinator
Prof. Salvatore Capozziello

XXX cycle - 2014/2017

Introduction

In 1962 Brian Josephson predicted the existence of a non dissipative current between two superconducting electrodes separated by an insulating barrier. Since then, the so-called Josephson effect has been extensively studied and applied in many fields, ranging from SQUID magnetometry to RSFQ circuits used as digital-RF receivers for signal intelligence applications. More recently, superconducting circuits have been proposed for application in energy-efficient computing systems and for the realization of auxiliary circuits for control and read-out of qubit circuits because of their unique properties.

In this work we study a particular kind of Josephson device, namely ferromagnetic Josephson junctions. Such systems have been extensively studied in the last 15 years because of the new physics arising from the interplay of two competing order parameters, i.e. the superconducting phase coherence and the long range correlations in ferromagnets. Ferromagnetic materials are characterized by long range correlations which tend to align all spins in the same direction. In conventional, s-wave superconductors the Cooper pairs are singlet pairs, with one spin up and one spin down electron and momentum $\pm\ k$. When a superconductor is brought into contact with a ferromagnetic layer, the Cooper pair acquires a finite momentum, due to the effective exchange field of the ferromagnet. The finite momentum of the Cooper pair leads to a modulation of the decay of the superconducting order parameter when it penetrates into the ferromagnet. If the exchange field is uniform, the junction exhibits specific behaviors, such as 0-π transitions and oscillating T_C and I_C as a function of the barrier thickness (see chapter 2). In the case of non uniform exchange field, more exotic phenomena occur, as for instance long range correlations, well beyond the ferromagnetic coherence length, have been observed. Such long range components of the supercurrent are triplet Cooper pairs with $S_Z = \pm 1$, insensitive to the exchange field of the ferromagnet.

In this PhD work I have carried out a comparative study of different ferromagnetic Josephson junctions. These last exploit the magnetic barrier in slightly different manners, covering complementary aspects of the physics

and functionalities of ferromagnetic junctions.

In the first experiment, in collaboration with Hypres Inc. and Russian ISSP, we study SIsFS junctions with Nb electrodes, and $Pd_{0.99}Fe_{0.01}$ as soft ferromagnetic barrier. The presence of an insulating layer of Al/AlO_x and a thin Nb interlayer guarantees higher critical current when compared to other SIFS junctions, and low dissipation compatible with Single Flux Quantum (SFQ) logic. This type of junction has already demonstrated to be suitable for the realization of magnetic random access memories (MRAM) compatible with existing superconducting circuits. The innovative idea is the possibility to act on the magnetic switch through a RF control. We report the effect of RF fields on magnetization switches in magnetic Josephson junction for the first time. We have performed a complete characterization of the enhancement in the separation of current levels representing the logical states, achieved by tuning magnetic field, temperature, RF frequency and energy.

In the second experiment, in collaboration with the Materials Science group of the University of Cambridge, a GdN ferromagnetic barrier gives special spin filter properties to the junction. We have given proof of a truly low dissipative nature of these devices through very low temperature measurements of switching current distributions (SCDs), and envisaged some criteria of how a careful analysis of phase dynamics can be indicative of unconventional processes, such as possible long-range triplet correlations. This analysis is made possible by a comparative study of a set of samples fabricated in a single fabrication run under the same deposition conditions, with a barrier thickness ranging from 1.5 nm to 4 nm. Characteristic junction parameters such as the critical current I_C and the normal state resistance R_N show specific trends. In addition, the whole IV curves show systematic behaviors pointing to possible fingerprints of exotic mechanisms. We measured the temperature behavior of the critical current of high spin filter efficiency junctions, down to 0.3 K, which is compatible with the presence of spin triplet correlations.

These two experiments exhibit not only some standard common behaviors of a ferromagnetic junction, but also two key features, as high values of $I_C R_N$ product and underdamped nature of the junctions. The combination of these two aspects will be crucial in the development of a new generation of supercomputers, aiming to solve both the energy efficiency issue and to integrate ferromagnetic junctions in spintronic and quantum circuits.

In this work, after a brief overview of the main theoretical aspects of Josephson junctions and of ferromagnetic systems in Chapter 1, we describe our low-noise experimental setup in Chapter 2. In Chapter 3 we will present our results on SIsFS Josephson memories. After a general characterization down to 0.3 K, we will focus on the effect of RF fields on switching processes.

In Chapter 4 we will review the current state of the art on spin filter junctions, and then we will show our results on high spin filter efficiency samples. In particular, we will present for the first time $I_C(T)$ curves down to 0.3 K for these samples, and our current progresses on the modeling of anomalous behavior of such curves.

Contents

Chapter 1

Josephson effect and magnetism

1.1 General features in conventional junctions

A Josephson junction is a device consisting of two weakly coupled superconductors, where the weak link can be a thin insulating layer, a metal or a physical constriction that locally weakens superconductivity such as a narrow superconducting bridge. It was predicted by Brian Josephson [1] that a non dissipative current can flow in such a device, due to the coherent tunneling of Cooper pairs. In absence of an applied voltage the supercurrent depends solely from the phase difference φ between the two electrodes, according to the first Josephson equation

$$I = I_{C_0} \sin \varphi \tag{1.1}$$

The first Josephson equation defines the current-phase relation of the device, which determines its fundamental properties.

In case of unconventional systems, this equation should be generalized in order to take into account also higher harmonics[2]

$$I(\varphi) = \sum_{n \geq 1} I_n \sin(n\varphi) \tag{1.2}$$

If the phase difference between the two superconducting electrodes changes with time, and so its time derivative is non zero, a voltage difference appears between the superconducting electrodes[3], according to the second Josephson equation

$$\frac{d\varphi}{dt} = \frac{2e}{\hbar} V \tag{1.3}$$

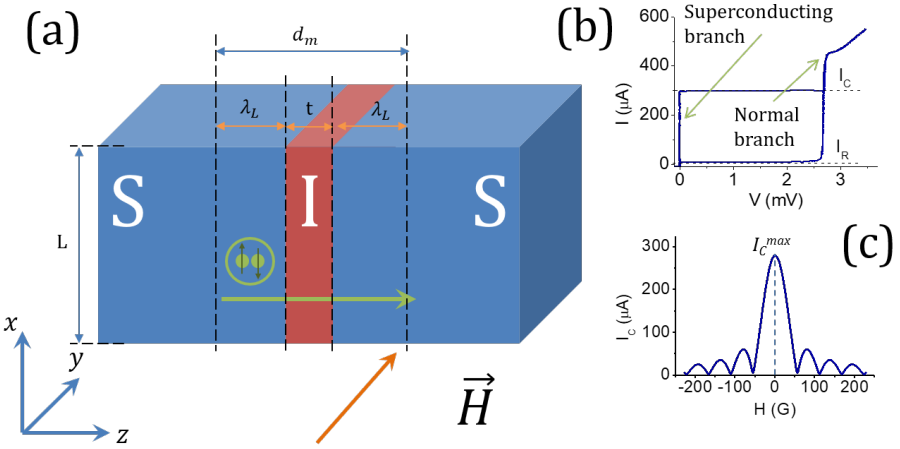

Figure 1.1: (a) Scheme of a standard Josephson junction in presence of a magnetic field along y direction. The non-dissipative supercurrent is due to tunneling of Cooper pairs through the barrier. (b) Sample I-V curve for a standard Josephson junction (Nb/Al-AlO_x/Nb junction from Hypres, Inc., experimental data). I_C is the critical current, I_R is the retrapping current. (c) Sample I_C(H) curve (experimental data from Nb/Al-AlO_x/Nb junction from Hypres, Inc.)

The phase difference between the electrodes can be modulated by external magnetic fields applied in the plane of the junction. In this case, the phase difference assumes a spatial dependence of the form

$$\varphi(x) = \frac{2e}{\hbar c} d_m H_y x + \varphi_0 \tag{1.4}$$

where d_m is the magnetic thickness, given by $d_m = t + \lambda_{L_1} + \lambda_{L_2}$ (see fig. 1.1 a), where λ_1 and λ_2 are the London penetration depths in the two superconducting electrodes and φ_0 is the phase difference for $x = 0$. Substituting eq. 1.4 into eq. 1.1 and maximizing with respect to φ_0 one obtains the conventional $I_C(H)$ dependence for a rectangular Josephson junction, which follows a Fraunhofer diffraction pattern

$$I_C(H) = I_C^{max} \left| \frac{\sin\left(\pi \frac{\Phi}{\Phi_0}\right)}{\pi \frac{\Phi}{\Phi_0}} \right| \tag{1.5}$$

where Φ is the magnetic flux and $\Phi_0 = \dfrac{h}{2e}$ is the flux quantum[3] (see fig. 1.1 b).

This description holds true in the *short junction* limit, when the self field due to external current flowing is negligible [3, 4]. The length scale that is used to discriminate between *short* and *long* junctions is the Josephson penetration depth λ_J, defined as

$$\lambda_J = \sqrt{\frac{\Phi_0}{2\pi\mu_0 J_C d_m}} \tag{1.6}$$

where d_m is the magnetic thickness and J_C is the critical current density. If the electrodes are thicker than the London penetration depth ($d_{1,2} > \lambda_{L_{1,2}}$), then

$$d_m = t + \lambda_{L_1} + \lambda_{L_2} \tag{1.7}$$

where t is the barrier thickness For junctions with $d_{1,2} < \lambda_{L_{1,2}}$, the magnetic thickness is given by

$$d_m = t + \lambda_{L_1} \tanh\left(\frac{d_1}{2\lambda_{L_1}}\right) + \lambda_{L_2} \tanh\left(\frac{d_2}{2\lambda_{L_2}}\right) \tag{1.8}$$

Thus, a Josephson junction falls in the short limit if $L/\lambda_J < 1$ and in the long limit if $L/\lambda_J > 1$, where L is a characteristic dimension of the junction.

The characteristic Cooper pair size is the superconducting coherence length ξ_S, which ranges from tens of angstrom to hundreds of nm.

1.2 AC Josephson effect

When a constant voltage $V \neq 0$ is applied to a Josephson junction, the total supercurrent flowing in the device is obtained by integrating eq.1.3 and substituting the result in eq.1.1[3]:

$$I = I_C \sin\left(\varphi_0 + \frac{2e}{\hbar} V t\right) \tag{1.9}$$

This supercurrent is an alternating current with a frequency $\omega_0 = 2\pi\nu_0 = \frac{2eV}{\hbar}$. The ratio between frequency and voltage is constant and is given by

$$\frac{\nu_0}{V} = \frac{2e}{h} = 483.6 MHz/\mu V \tag{1.10}$$

This is called the *a.c. Josephson effect*. The experimental observation of this phenomenon is possible in presence of microwave irradiation of a junction biased with a d.c. current. In this case, the interaction between

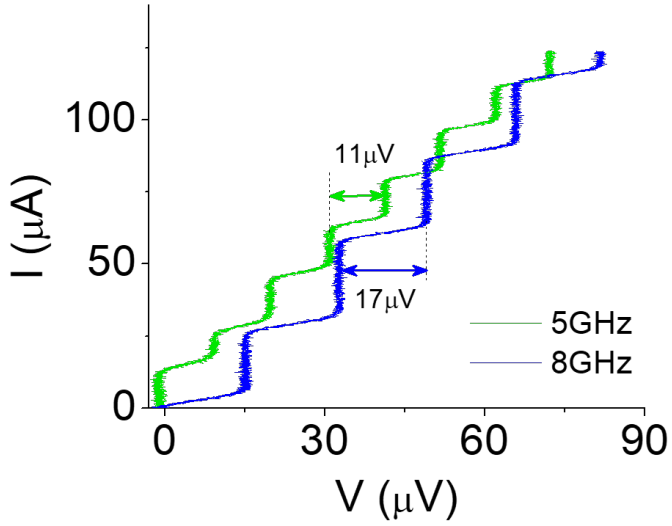

Figure 1.2: Experimental Shapiro steps observed at different microwave frequencies for a Nb/Al-AlO_x/$Pd_{0.99}Fe_{0.01}$/Nb junction

the microwave signal and the a.c. Josephson current leads to the appearance of current steps at constant voltages (see fig.1.2). Such steps have been observed for the first time by Shapiro[5] in 1963 and thus are called *Shapiro steps*. These steps occur at

$$V_n = \frac{nh}{2e}\nu_0 \tag{1.11}$$

where n is an integer number.

1.3 Phase dynamics

A Josephson junction in an external circuit can be modeled as an ideal Josephson junction in parallel with a resistance R and a capacitance C, according to the Resistively and Capacitively Shunted Junction (RCSJ) model (Fig.1.3). The balance equation for this circuit is simply

$$I = I_C \sin\varphi + \frac{V}{R} + C\frac{dV}{dt} \tag{1.12}$$

It can be seen that using eq. 1.1 and 1.3 the balance equation for the circuit is equivalent to the motion equation of a phase particle moving in a *tilted*

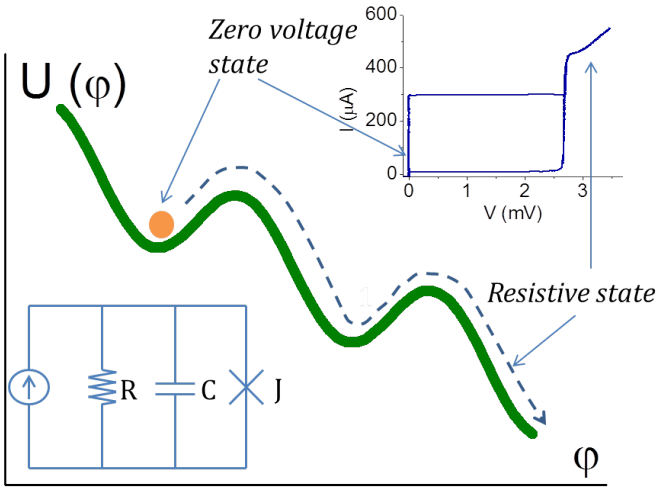

Figure 1.3: Main figure & upper right inset: washboard potential for the phase particle. When the phase particle (orange circle) oscillates in one of the minima of the potential, the junctions is in its superconducting zero voltage state. When the phase particle rolls down the washboard potential, the junction is in the resistive state. Lower left inset: RCSJ equivalent circuit for a real Josephson junction

washboard potential and subject to a viscous force.

$$\frac{d^2\varphi}{dt^2} + \frac{1}{Q}\frac{d\varphi}{dt} + \sin\varphi = \frac{I(\varphi)}{I_{C_0}} \tag{1.13}$$

The *tilted washboard potential* is given by

$$U(\varphi) = \frac{\hbar I_{C_0}}{2e}\left(1 - \cos\varphi - \frac{I}{I_{C_0}}\varphi\right) \tag{1.14}$$

The prefactor Q is called damping factor, and is defined as

$$Q = \omega_P RC \tag{1.15}$$

where $\omega_P = \sqrt{\frac{2eI_C}{\hbar C}}$ is the *plasma frequency*. As can be seen, Q has a strong dependence on the capacitance C. Following the analogy with the motion of a phase particle, a system with $Q < 1$ is called overdamped, while when $Q \gg 1$ the system is underdamped. In the first case, the capacitance is small, the second derivative term in eq. 1.13 can be neglected and the equation can be solved analytically, obtaining a non hysteretic current-voltage (IV) characteristic.

The small capacitance is typical of Josephson junctions with a non-insulating, metallic barrier. On the other hand, when the barrier is a dielectric the capacitance C is high, and so is Q. In this case eq. 1.13 must be solved numerically and the IV curve is hysteretic. Using the tilted washboard potential model (eq. 1.14) the phase dynamics can be schematized as follows (fig. 1.3):

- for $I < I_C$ the phase particle is trapped in a minimum of the washboard potential. This corresponds to the zero voltage branch of the IV curve.
- Increasing the bias current for $I \geq I_C$ the phase particle escapes from the potential well and starts rolling down the washboard potential. This corresponds to the resistive branch of the IV curve, which is ohmic.
- When decreasing the bias current, the particle remains in a non-ohmic resistive state that corresponds to the quasiparticle branch of the IV curve. The phase particle remains in this state until the current reaches a certain value, called retrapping current, which is smaller than the critical current I_C.
- For $I < I_r$ the particle is trapped again in a minimum of the potential, thus returning to the superconducting branch.

The escape and retrap of the phase particle are both stochastic processes, governed by specific probability distributions [6]. The escape events can be collected in an histogram using a specifically designed low-noise setup (see sec. 2.1.1, 2.2.1). The analysis of these histograms using well-know probability distribution functions[6, 7, 8] allows the study of the transition between different escape regimes [9, 10, 11]. The analysis of first and second moments of the distribution (the mean switching current I_{mean} and the distribution width σ) enables to determine not only the phase dynamics of a junction, but also the electrodynamical parameters that come into play when the junction is embedded in a circuit.

1.3.1 Underdamped regime

In this and in the following sections we will focus only on escape events. We have already seen that such processes in underdamped junctions are stochastic processes, and can be interpreted as the motion of a phase particle in a washboard potential. The escape of such particle from one of the minima can be either thermal or quantum. In the first case, thermal fluctuations excite the phase particle above the energy barrier, causing the switch to the

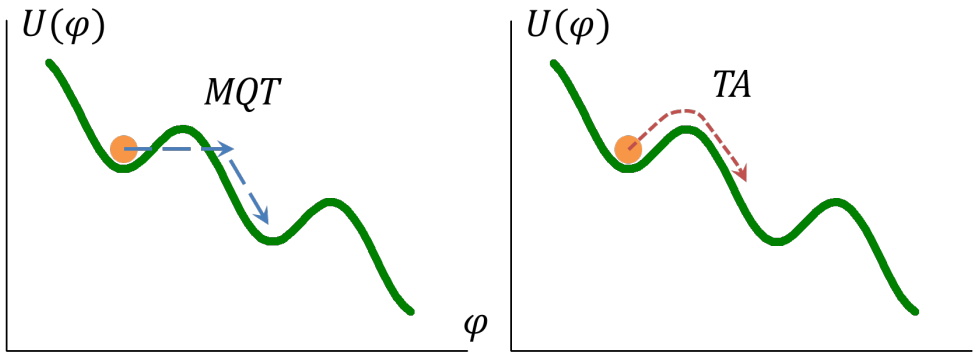

Figure 1.4: Schematic representation of escape processes in a Josephson junction. Left: thermal activation regime. The main contribution to escape events comes from thermal fluctuations that excite the phase particle above the energy barrier. Right: macroscopic quantum tunneling regime. In this case, the tunneling through the energy barrier dominates the escape processes.

resistive state. In case of quantum tunneling, the phase particle tunnels through the barrier and goes into the resistive state (fig. 1.4).

Typically, for low dissipation junctions ($Q \gg 1$) a single escape event is enough to switch the junction in the running state. The saturation of both I_{mean} and σ below a certain temperature T_{cross} indicates the transition from a thermal escape (TA) regime to a macroscopic quantum tunneling (MQT) regime [6] (see fig.1.5). The transition temperature is given by [12]

$$T_{cross} = \left(\frac{\hbar\omega_p}{2\pi k_B}\right)\left[\left(1+\frac{1}{4Q^2}\right)^{1/2} - \frac{1}{2Q}\right] \tag{1.16}$$

For underdamped junction, the factor $\left[\left(1+\frac{1}{4Q^2}\right)^{1/2} - \frac{1}{2Q}\right]$ is very close to unity, and almost independent from Q. This allows a self-consistent calculation of the RCSJ junction parameters.

External magnetic field is used as an in-situ knob to change T_{cross}, and subsequently the saturation of the distribution width at lower temperatures thus excluding saturation effects due to electronic noise or other external causes. According to eq. 1.5, the magnetic field modulation the critical current I_C. The critical current reduction brings a subsequent reduction in ω_P, and consequently in T_{cross}.

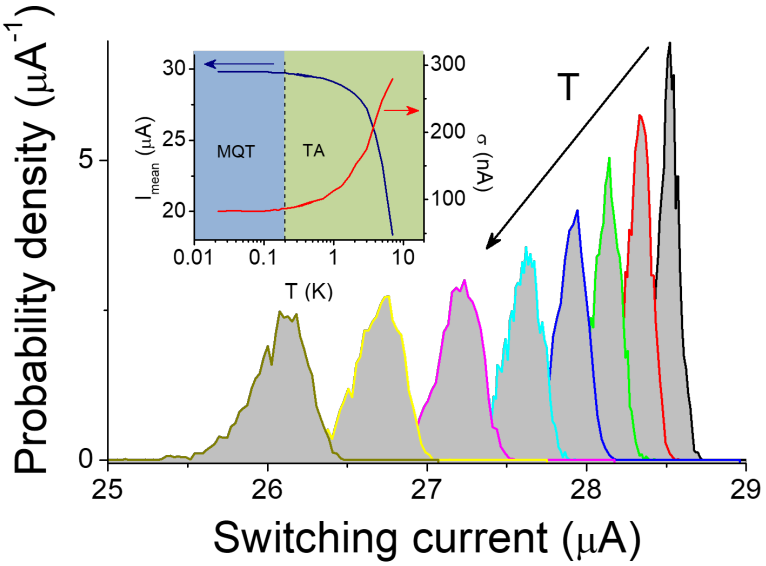

Figure 1.5: Switching current distribution for a $NbN/GdN/NbN$ junction in the underdamped regime, with $Q \sim 10$, barrier thickness $\sim 2.5nm$ and area $\sim 50\mu m^2$. The black arrow indicates the direction of increasing temperature. Inset: mean switching current (blue) and distribution width (red) as a function of temperature.

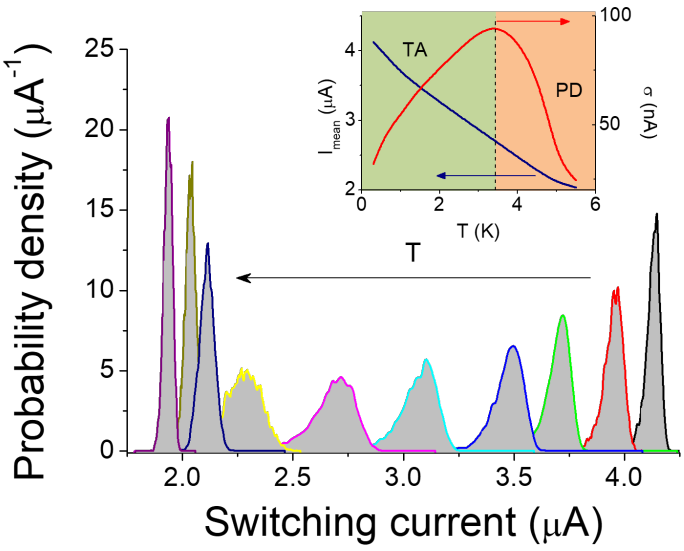

Figure 1.6: Switching current distributions in the moderately damped regime. The sample is a $NbN/GdN/NbN$ junction, with $Q \sim 5$, barrier thickness $\sim 3nm$ and area $\sim 50\mu m^2$. Inset: mean switching current and distribution width as a function of temperature

1.3.2 Moderately damped regime

For junctions falling in the overdamped regime ($Q < 1$), the phase particle can be retrapped in one of the following minima after an escape event. At low bias, escape and retrap can occur multiple times, generating phase diffusion and preventing the switch to the running state until the tilt of the potential is increased. In this case, a finite voltage appears in the IV characteristics [3, 7, 13], and the IV curve is no longer hysteretic with a resistive branch at low voltages. In this case, the transition to the running state is no longer a stochastic event.

It has been demonstrated long ago[7] that phase diffusion and hysteresis in IV curves can coexist in small area junctions, where this coexistence is explained in terms of frequency dependent damping in the framework of RCSJ model.

Phase diffusion has been observed also in junctions with $1 < Q < 5$, namely junctions falling in the moderate damping regime [10, 14, 15, 16, 17, 18]. In these devices, the usual crossover between TA and MQT is joined by the transition from TA to phase diffusion (PD). After the MQT saturation at low temperatures, the distribution width σ follows the predicted $T^{2/3}$ dependence for TA. After T^*, which is defined as the temperature where σ reaches

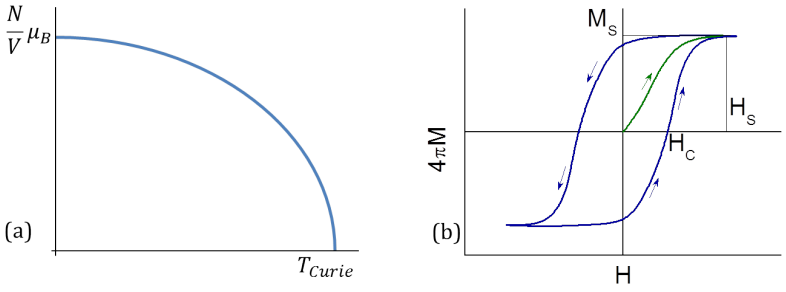

Figure 1.7: (a) Magnetization as a function of temperature. Above the Curie temperature T_{Curie} the material is paramagnetic. As temperature decreases the ferromagnetic ordering increases and so does the magnetization (b) Hysteresis loop for a ferromagnetic material. The green line is the first magnetization curve (also called virgin curve). The coercive field H_C is the field needed to bring back the material to zero magnetization. M_S is the saturation magnetization, and the field value at which magnetization reaches the saturation value is called saturation field H_S.

its maximum, the derivative of σ changes its sign and so the distribution width decreases with increasing temperature while the mean switching current decreases. Naively, one would expect that as the temperature increases, fluctuations in switching current increase and thus the distribution width increases as well. The anomalous behavior of the current distributions can be explained in terms of a competition between thermal escape and multiple retrapping processes: for $T < T^*$ the thermal escape dominates on retrapping, while for $T > T^*$ holds the opposite.

It has been demonstrated for grain boundary YBCO junctions with small critical current density J_C the direct transition between MQT escape processes and phase diffusion[10].

1.4 S/F systems

1.4.1 Ferromagnetic materials

Ferromagnetic materials are characterized by a phase transition below the Curie temperature T_{Curie}, where microscopic magnetic moments tend to align in the same direction, thus causing an overall magnetization of the sample. The typical temperature dependence of magnetization is sketched in fig. 1.7a. If an external magnetic field is applied, magnetization in ferromagnetic materials has a hysteretic behavior, as shown in fig. 1.7b.

The magnetization in ferromagnetic materials saturates to M_S when most of the microscopic magnetic moments are aligned. The external field for which the saturation begins is called *saturation field* H_S. The coercive field H_C is the external field needed to set the magnetization to zero. When the field is applied for the first time, M increases as H increases (green line in fig1.7b), then for field values above the *saturation field* H_S, the magnetization saturates to a certain value M_S. When coming back to low fields, M(H) describes a different curve, in particular, at zero external field the magnetization is finite. This magnetization value is called *residual magnetization*. Decreasing the field down to negative values, we reach the *coercive field* $-H_C$, at which the magnetization is zero. Further decrease of the magnetic field below $-H_S$ causes a saturation in the magnetization to $-M_S$. Increasing the field again, the magnetization increases accordingly, until it reaches zero at H_C. By further increasing the applied field, M increases up to the saturation M_S.

If the maximum applied field is $|H| < |H_S|$, then the magnetization loop is smaller than the one shown in fig. 1.7b. A series of magnetization loops with decreasing maximum applied fields is used to bring the specimen back to the virgin state. Alternatively, the same result is obtained heating above T_{Curie} [19].

1.4.2 Proximity effect in S/F bilayers

The superconductor/normal metal interfaces are described in terms of proximity effect, which is the reciprocal influence of a superconductor in contact with a metal or a ferromagnet, and more specifically for our aims the ability of transferring superconductivity into a normal metal. In S/N systems one observes a decrease of the critical temperature of the superconductor with respect to the bulk material as the thickness of the N layer increases[20]. At the same time, also a rise of a weak superconductivity in the normal metal is observed. The details of these effects depend on the actual boundary conditions of the system.

The S/N proximity effect can be roughly described by means of the Ginzburg-Landau theory.

In this framework the transition between the normal phase and the superconducting phase for a bulk material is a second order transition described by an order parameter whose value is respectively 0 and 1.

In the case of S/N interfaces one observes a smooth transition between the two phases and the energy functional for $T \approx T_c$ in this case can be

written as[21]

$$F_{GL} = a(T)|\psi|^2 + \gamma(T)|\nabla\psi|^2 + \frac{b(T)}{2}|\psi|^4 \tag{1.17}$$

Consequently, the linear Ginzburg-Landau equation for a S/N interface in one dimension is

$$a(T)\psi - \gamma(T)\frac{\partial^2\psi}{\partial x^2} = 0 \tag{1.18}$$

The solution of (1.18) is the simple decaying exponential shown in fig.1.8a [22]:

$$\psi = \psi_0 \exp\left(-\frac{x}{\xi_N}\right) \tag{1.19}$$

where $\xi_N = \sqrt{\gamma/a} = \sqrt{\gamma/\alpha(T - T_c)}$ is the characteristic decay length of the order parameter in the normal metal. This characteristic length represents the coherence length of the Cooper pairs within the normal metal, it sets the scale of the superconducting properties inside the barrier.

According to conventional BCS microscopic theory of superconductivity the Cooper pairs are made up of electrons with opposite spin [23], while in ferromagnetic materials the spins tend to be aligned in the same direction. It is thus clear that in a ferromagnetic junction we are in presence of two competing order parameters. Since energy scales for common strong ferromagnets such as Iron and Cobalt are much larger than the typical energy scales of superconductivity, one would expect a strong suppression of superconductivity in S/F bilayers. The typical energy scale for superconductivity is the superconducting energy gap, which is few meV. The typical exchange fields for a strong ferromagnet range from hundreds of meV to few eV[21, 24].

In 1964 Larkin and Ovchinnikov [25] and Fulde and Ferrel [26] predicted that in a pure ferromagnetic superconductor at low temperature superconductivity may be non uniform, showing a sinusoidal modulation of the order parameter at the scale of the superconducting coherence length (FFLO state). The appearance of a modulation in the superconducting order parameter is related to the Zeeman splitting of electronic levels due to exchange field. In absence of the exchange term a Cooper pair is formed by two electrons with opposite momentum and opposite spin. When exchange field is added, the spin up electron decreases its potential energy by an amount h and increases its kinetic energy by the same amount, while spin down electrons see an increase in potential energy and a decrease of the kinetic energy of the same amount h. The net result is a net momentum $2\delta k$ acquired by the Cooper pair, which implies a spatial modulation of the order parameter with a wave vector $2\delta k$ [21].

In order to apply Ginzburg-Landau theory to S/F interfaces, it is necessary to consider higher derivative terms in the expansion (1.17):

$$F_{GL} = a(T)|\psi|^2 + \gamma(T)|\nabla\psi|^2 + \frac{\eta(T)}{2}|\nabla^2\psi|^2 + \frac{b(T)}{2}|\psi|^4 \tag{1.20}$$

The linearized Ginzburg-Landau equation in 1D then becomes

$$a\psi - \gamma\frac{\partial^2\psi}{\partial x^2} + \frac{\eta}{2}\frac{\partial^4\psi}{\partial x^4} = 0 \tag{1.21}$$

If we assume a real order parameter in the superconductor, then the order parameter in the ferromagnet is also real, and assumes the form (fig. 1.8b)

$$\psi = \psi_0 \exp\left(-\frac{x}{\xi_{F1}}\right)\cos\left(\frac{x}{\xi_{F2}}\right) \tag{1.22}$$

where $\xi_{F1} = \left[\frac{|\gamma|}{2\eta}\left(\sqrt{1+\frac{T-T_{ci}}{T_{ci}-T_{cu}}}-1\right)\right]^{-1/2}$ and $\xi_{F2} = \left[\frac{|\gamma|}{2\eta}\left(1+\sqrt{1+\frac{T-T_{ci}}{T_{ci}-T_{cu}}}\right)\right]^{-1/2}$. T_{cu} is the transition temperature of the system into the uniform superconducting state and T_{ci} is the transition temperature into the non-uniform superconducting state. These two transition temperatures are related to the parameter a by the relation $a = \alpha(T_{ci} - T_{cu})$[21].

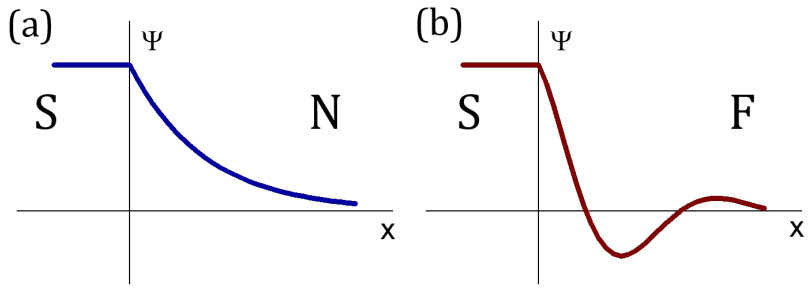

Figure 1.8: (a) Superconducting order parameter at S/N interface. (b) Superconducting order parameter at S/F interface. The exchange field causes an oscillation of the order parameter

However, one should keep in mind that in real ferromagnetic junctions the gradients of the superconducting parameter are large because of the large exchange field compared with the superconducting energy scales, so the Ginzburg-Landau theory cannot describe properly these systems and a microscopical approach is required. The most convenient scheme is the Bogoliubov-de Gennes equations or the Green's functions using the quasiclassical Eilenberger or Usadel equations [27],[28].

There are no experimental evidences of FFLO state in bulk superconductors, but they have been observed in artificially fabricated superconductor/ferromagnet multilayers (see [21] and [24] for an overview of experimental and theoretical results).

In ferromagnetic junctions the damped oscillatory behavior of the order parameter is responsible for many interesting effects, which are peculiar for SFS junctions, such as $0-\pi$ transitions depending on the F layer thickness. A π junction is a Josephson junction in which the phase difference of the electrodes in the ground state is π instead of 0. In this case the critical current I_C in (1.1) is negative instead of being positive as in the 0 phase, which is the the ground state for a conventional junction. This effect was already predicted in the late seventies[29], and demonstrated experimentally in early 2000s[30, 31, 32, 33, 34, 35]. As an example, consider a F layer of thickness smaller than ξ_{F2}. The wave function in the F layer slightly changes and the superconducting order parameter in the adjacent S layer remains the same. In this case the phase difference between the superconducting order parameters in the S layers is absent and the junction is in the 0 phase. If we now consider a F layer of thickness $\sim \xi_{F2}$, the pair wave function may cross zero at the center of the F layer. This causes a π shift of the phase of the superconducting order parameter in the adjacent S layers so that the junction is in the π phase. The characteristic thickness of the F layer corresponding to a the transition from the 0 to the π state is $\xi_{f2} = \sqrt{D_{f2}/h}$ and it is rather small in typical ferromagnets (10-50 Å) because of the large value of the exchange field $E_{exch} \approx 1000K$. The theoretical predictions are confirmed by a great amount of experiments [30, 31, 32, 33, 34, 35].

Since the current-phase relation in ferromagnetic junctions is sinusoidal only in the vicinity of T_C, higher harmonic terms can be significant in the vicinity of $0-\pi$ transition, where the critical current for the first harmonic vanishes. The presence of a second harmonic term in the current-phase relation will be discussed with greater detail in chapter 4. It should be noted however, that this term dramatically affects the washboard potential, thus heavily influencing the phase dynamics of a junction. In presence of a second harmonic CPR the washboard potential becomes[36]

$$U(\varphi) = \frac{\hbar I_{C_1}}{2e}\left[\frac{I_{bias}}{I_{C_1}}\varphi + (1-\cos\varphi) + \frac{g}{2}(1-\cos 2\varphi)\right] \tag{1.23}$$

where g is the ratio between the first and second harmonic critical currents. In this case, the periodic potential shows two minima at different φ, depending on the sign of g (fig.1.9): when the second harmonic is positive (red lines in fig1.9), the washboard potential has two non degenerate minima at $\varphi = 0$ and $\varphi = \pi$, so the junction can be in the 0-phase or in the π-phase,

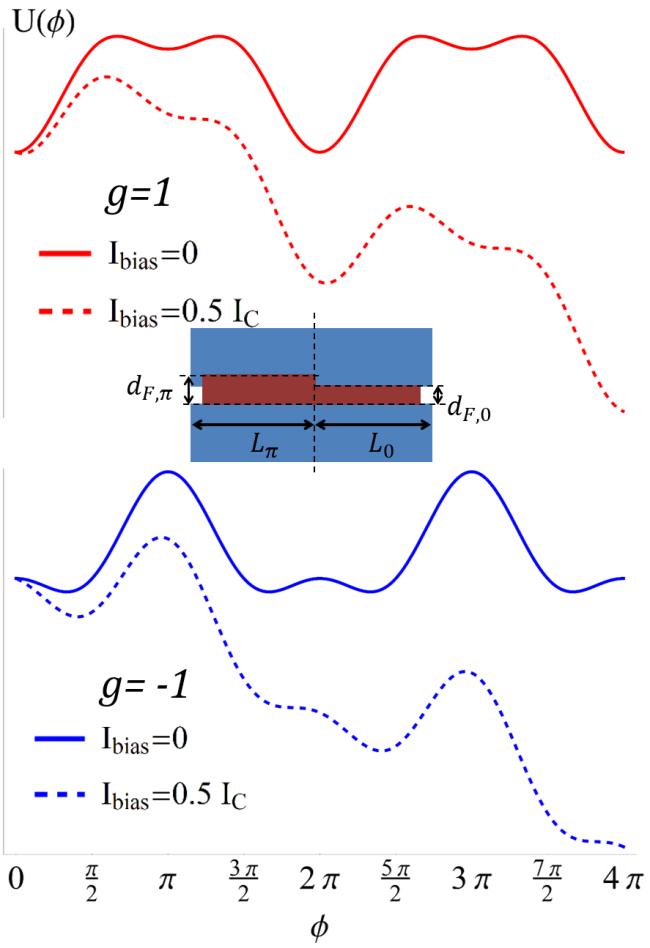

Figure 1.9: Washboard potential for $g = \pm 1$, in absence and in presence of external bias current

with different critical currents, depending on damping conditions and other parameters [9, 36]. When the second harmonic contribution is negative (blue lines in fig1.9), the junction has two degenerate minima at $\varphi = \pm\phi_0$, with two different critical currents. This is the case of φ-junctions[36, 37].

1.4.3 Long range proximity effect

The φ-junctions described in the previous section are a particular type of non-homogeneous ferromagnetic junction. Experimentally, φ-junctions are fabricated using two different thicknesses of the ferromagnetic layer in the same junction (see inset in fig.1.9)[37].

In all cases where the exchange field is non-homogeneous, other and much more "exotic" phenomena can be observed. Such an exchange field causes a non trivial spin structure, where also a triplet component ($S = 1$, $S_Z = 0, \pm 1$) is present in the superconducting condensate. This component is not destroyed by the exchange field in the ferromagnet, but can propagate inside the barrier over distances comparable to the coherence length in normal metals. This effect is thus called *long range proximity effect*[24]. Non-zero critical currents have been observed in Josephson junctions with barrier thicknesses far larger than the decay length of singlet pairs in ferromagnets [38, 39, 40, 41].

The overall wave-function of the condensate must be anti-symmetric, as a consequence of the Pauli principle, so the Gor'kov function describing the triplet state in conventional (s-wave) superconductors has to be an odd function of the Matsubara frequency, for this reason this kind of superconductivity is called *odd triplet superconductivity*. Recently, odd triplet gapless states have been observed in S/F bilayers[42], while triplet supercurrents have been reported also in hybrid ferromagnetic Josephson junctions [43]. Triplet superconductivity has been reported also in superconducting spin valves [44].

There are several theoretical works describing the effect of triplet correlation in experimental data, both in diffusive[45, 46] and ballistic[47, 48, 49] regimes. The two main ingredients for the formation of long range triplet Cooper pairs are the spin mixing, and the triplet rotation[45]. The spin active interface provides the spin polarization needed to turn a singlet pair ($S = 0$, $S_Z = 0$) into a triplet pair with $S_Z = 0$, while the rotation of $S = 1$, $S_Z = 0$ Cooper pairs into $S_Z = \pm 1$ pairs is due to misalignment of the interface magnetic moments with respect to the bulk magnetization. Also in [47] the spin polarization plays a fundamental role, but in this case the spin mixing is provided by the misalignment between the exchange field induced into the superconducting electrodes by the ferromagnetic barrier and the magnetization of the barrier itself. From $I_C(T)$ expression calculated for such ballistic

systems, it can be readily seen that long-range triplet components become important only for large spin polarization values. The presence of such components in the critical currents causes a huge deviation from standard $I_C(T)$ behavior and the appearance of subgap features in conductance spectra.

1.4.4 Josephson magnetometry

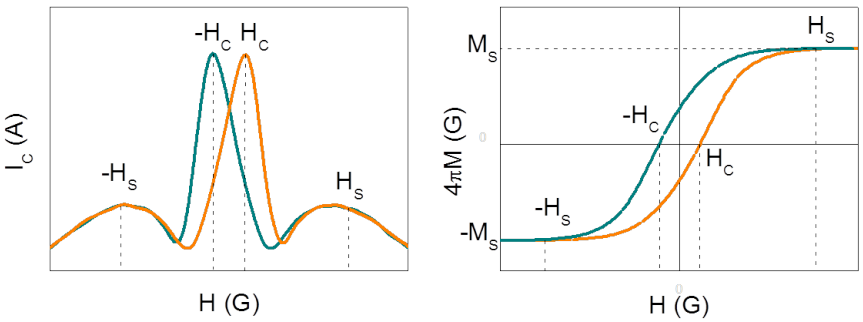

Figure 1.10: Magnetization curve obtained from $I_C(H)$ dependence using Josephson magnetometry [50]

If the coercive field H_C and the saturation field H_S are sufficiently small, and the saturation magnetization M_S is sufficiently large, the presence of a ferromagnetic barrier within a Josephson junction is immediately seen from the $I_C(H)$ dependence. In this case, depending on the magnetic field sweeping direction, one observes that $I_C(H)$ curves are shifted and distorted. In particular, when the magnetic field is ramped from negative to positive values, the maximum of the Fraunhofer pattern is shifted towards positive fields, while it is shifted toward negative values of the magnetic field when the external field goes from positive to negative values. This distinctive behavior of junctions with soft ferromegnetic barriers reflects the M(H) curve of the ferromagnet (see fig.1.10).

When a ferromagnet is embedded in a Josephson junction as barrier, a direct measurement of M(H) curve is not always possible. If the magnetic sample is uniform, one can reconstruct M(H) from $I_C(H)$ using the methods described in [50].

For a standard $I_C(H)$ dependence as the one given in (1.5), the maxima

and minima of critical current are determined by

$$\Phi^{min} = \Phi_0 m \tag{1.24}$$

$$\tan \frac{\pi \Phi^{max}}{\Phi_0} = \frac{\pi \Phi^{max}}{\Phi_0} \tag{1.25}$$

$$\Phi^{max} \approx \Phi_0 (n + 1/2) \tag{1.26}$$

where m and n are integers. The magnetic flux Φ_M due to the ferromagnetic layer magnetization M adds up to the flux generated by the external field Φ_H

$$\Phi = \Phi_M + \Phi_H = 4\pi M L d_F + H L d_m \tag{1.27}$$

where L is the junction width, d_F is the thickness of the ferromagnetic layer and d_m is the magnetic thickness[4] of the junction. Using these relations it is possible to transform $I_C(H)$ into $\Phi(H)$ dependence, and then into $M(H)$.

The M(H) curve thus obtained is affected by large uncertainties due to approximation in the procedure, but still gives a good estimate of M(H) parameters such as coercive field H_C and saturation field H_S, which will be useful in the following.

Chapter 2

Experimental setup

2.1 Evaporation cryostat

All experimental measurements in this work have been performed using a Heliox VL evaporation cryostat from Oxford instruments, with customized low noise filters.

During the measurements, the cryostat is sealed and vacuum is created inside the inner vacuum chamber (IVC). The cryostat is dipped in a ^{4}He bath and uses a ^{3}He closed dump to reach a base temperature of about 0.3K. A thin capillar draws ^{4}He from bath to the 1K pot, where it is pumped in order to reach a temperature around 1.8K. At this temperature ^{3}He gas in the ^{3}He pot liquefies. The 0.3K base temperature is reached by pumping on the ^{3}He pot with the sorption pump, a zeolitic material which is active below 30K. The sample is mounted at the bottom of ^{3}He and thermally anchored to it. A scheme of the cryostat is sketched in fig. 2.1.

Magnetic field up to 0.3T can be applied through a superconducting Niobium-Titanium coil thermally anchored to the 1K pot, so that the coil remains in the superconducting state regardless of ^{3}He pot temperature, also reducing the thermal load on the cold finger of the cryostat.

2.1.1 Filtering system

The observation of quantum properties of superconducting systems requires specific arrangement to attenuate thermal and electronic noise. A careful choice of the materials used for wires and a stable thermal anchorage are fundamental to reduce thermal noise; electronic noise is reduced by specific filtering stages and by a common stable ground for all electronics[51, 52]. All signals pass through a low-noise, battery-powered amplifier connected to

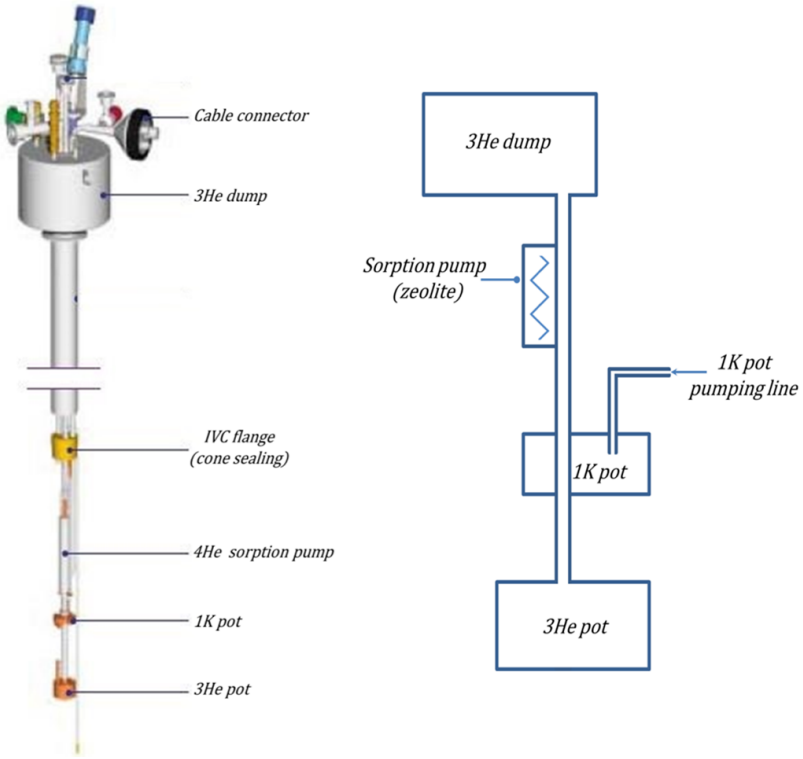

Figure 2.1: Evaporation cryostat used for measurements. Right: simplified scheme of the cryostat. ^{3}He gas is in a closed dump, cooled down to 1.8 K when passing through the 1K pot. The ^{3}He pot is where the condensation takes place and the base temperature of 0.3 K is reached. The temperature control of the ^{3}He pot is performed using either a zeolitic sorbtion pump and a controllable resistor placed close to the ^{3}He pot.

the electrical lines of the cryostat, in order to decouple them from external environment.

Voltage-carrying lines from room temperature electronics to 1K pot are manganine wires, an alloy of Copper, Manganese and Nickel with a small thermal conductivity at low temperatures. Current-carrying lines are Copper wires, which has a lower resistance with respect to manganine and so reduces heating. Lines from 1K pot stage to 0.3K stage are superconducting Niobium-Titanium cables, which can carry large currents without any temperature increase of the sample anchored to the cold stage.

The first filtering stage designed to reduce electrical noise consists in room temperature EMI filters. The second filtering stage is thermally anchored to the 1K pot, and consists of a RC circuit for each line (8 lines in total), with R= 100 Ω and C= 1 nF. These filters are low pass filters with a cut-off frequency of about 1 MHz. For higher frequency the parasitic inductance of the capacitors causes a significant loss in attenuation [52]. The last two filtering stages are anchored to the 1K pot and ^{3}He pot respectively, and consist of a copper powder filters, with a cut-off frequency of few GHz. These filters are coils of insulated wire inside a tube filled with copper powder with a grain size of a few μm. Each grain is insulated from the others by a naturally grown oxide layer, and each couple of grains can be seen as a single capacitor. The effective area of the resulting capacitance is thus very large.

The dewar has a double screening system for magnetic fields: an external cryoperm screen, which is a Nickel-Iron alloy with high permeability and an inner superconducting screen. Each screen won't be sufficient for an efficient screening: on one hand, the cryoperm screen would be magnetized by the high fields applied to the sample, on the other hand the superconducting screen might trap external field during the cooling down phase.

2.2 Dilution refrigerator

In order to fully determine the phase dynamics of the devices presented here, we rely on results previously obtained for similar junctions. In particular, we use the junction parameters obtained for samples with $I_C \approx 30\mu A$ reported in [9] as a comparison term for the parameters estimated for junctions with lower critical currents. The measurements reported in [9] have been performed in a Kelvinox400MX dilution refrigerator from Oxford Instruments. Here we present a brief overview of the functioning principles of this cryostat, which will be used in the near future to characterize samples with spin filter efficiency of $>$95% and critical currents ranging from few μA down to few hundreds of nA down to 20mK.

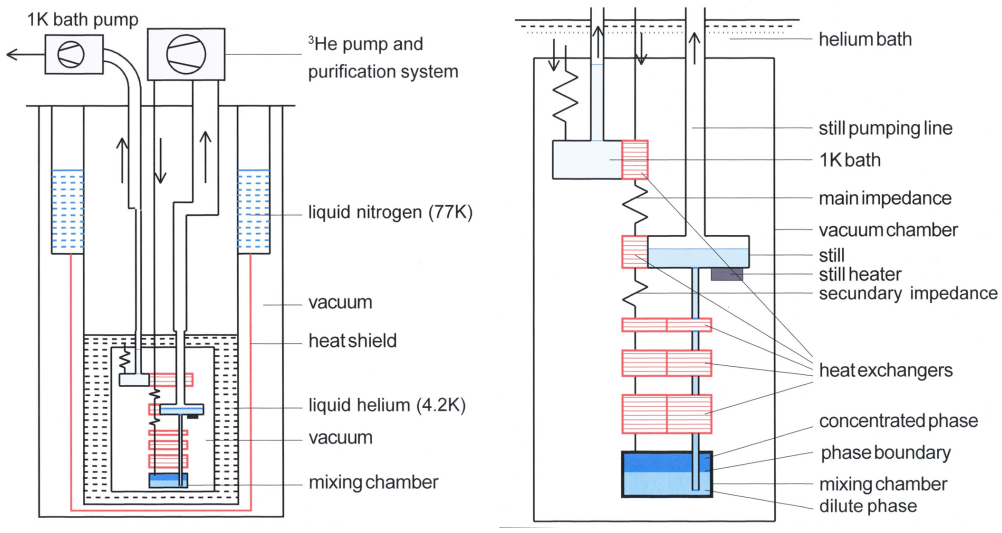

Figure 2.2: Schematic representation of a dilution cryostat. Left: overview. Right: details of the coldest part of the cryostat.

The base temperature is reached using a ^{3}He-^{4}He mixture and an experimental setup first proposed by Heinz London in the early 1950s. The ^{3}He gas is purified and precooled by liquid nitrogen at 77 K, then it is further cooled by a ^{4}He bath at 4.2 K. Then it is further cooled below 2 K by means of a pumped ^{4}He bath, as in the evaporation cryostat. At this temperature ^{3}He liquefies. Then the working fluid enters a capillary with a large flow resistance called *main impedance* and it is cooled by the *still* to a temperature of about 600 mK. At this point ^{3}He passes through a *secondary impedance*, then it is cooled by a cold flow of ^{3}He coming from the *mixing chamber*. Finally it enters the mixing chamber, which contains the ^{3}He-^{4}He mixture.

Below 800 mK this mixture undergoes a spontaneous phase separation, see fig. 2.3. In the mixing chamber the concentrated phase and the dilute phase are in equilibrium and separated by a phase boundary. The cooling power is provided by the heat of mixing of the two isotopes since the process of moving ^{3}He through the phase boundary is endothermic and removes heat from the mixing chamber environment.

The ^{3}He of the dilute phase of the mixture at about 20 mK leaves the mixing chamber and on its way up cools down the downward flowing ^{3}He coming from secondary impedance. Then it reaches the still, where it is heated. The vapor in the still is practically pure ^{3}He, so there is an osmotic pressure between the mixing chamber and the still which drives more helium from the concentrated to the dilute phase in the mixing chamber, and up to

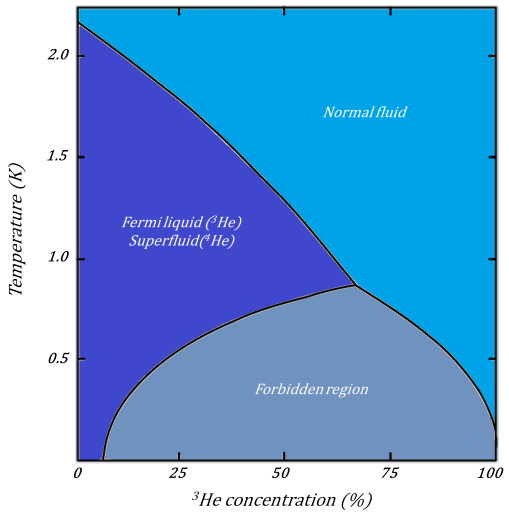

Figure 2.3: Phase diagram of ^{3}He-^{4}He mixture

the still.

Finally, the pumps compress the ^{3}He to a pressure of a few hundred millibar and feeds it back into the cryostat, completing the cycle.

2.2.1 Filtering system

The filtering stages of the dilution refrigerator are very similar to the ones of the evaporation cryostat. First of all, also in this case a stable ground is provided and all the electronics have been connected to it. The electrical lines from room temperature electronics to the sample stage are 12 twisted pairs, each one shielded by a German silver (a Copper-Nickel-Zinc alloy with low thermal conductivity) tube. From room temperature to the 1K pot, the wires are both manganine and copper ones, as in the case of the evaporation cryostat. At the room temperature stage, electromagnetic interference filters have been mounted in order to reduce electromagnetic high frequency peaks such as the ones coming from mobile phones. The next filtering stage is thermally anchored to the 1K pot and consists in 12 $RLC - \pi$ filters, one for each line. In this case the cut-off frequency for these devices is 100 kHz. The wiring from the 1K pot to the mixing chamber is made with Niobium-Titanium superconducting wires with a critical temperature of 11 K. This allows the sample biasing without excessive heating. The π filters are not enough, so a further filtering stage is provided combining copper powder and twisted pairs. The first copper powder filter is linked to the cold plate (about 50 mK), the second is thermally anchored to the mixing chamber.

Magnetic field measurements are possible also with this setup, since a superconducting Niobium-Titanium coil is mounted at the sample stage and thermally anchored to the still to avoid heat load on the mixing chamber. The maximum field value is 50 mT.

A screening system has been provided to shield the setup against magnetic field. The outer one is a 1mm thick cryoperm screen, the second is a lead shield 1mm thick and the inner one is a μ-metal screen.

2.3 Electronic setup

The electronic setup connected to the evaporation cryostat allows different kinds of measurements in order to characterize different types of devices.

All measurements are performed using a four wire connection using Aluminum wires, in order to exclude all the contribution to the resistance not due to the sample (lines, electrodes, etc)

The junctions are current biased using an Agilent 33120A arbitrary waveform generator. The generated voltage difference passes through a unitary gain amplifier that decouples it from external noise and then goes on a tunable shunt resistance, usually much larger than the lines impedance, so that the measured device is current biased. Since a return current path is provided, it is also possible to measure directly the current passing through the junction. The measured output signal is the voltage across the junction, amplified using a variable gain amplifier included in the battery powered decoupling unit. The frequency of the input signal is always chosen far from 50 Hz in order to avoid resonance effects with electricity grid.

Current versus voltage characteristics can be measured as a function of temperature and/or magnetic field, in order to obtain a wide characterization of the sample. Magnetic field is generated using a source meter Keithley 2400 connected to the superconducting coil. Temperature is controlled using a resistor placed on the cold stage of the cryostat.

Resistance versus temperature measurements are crucial for spin filter Josephson junctions to estimate spin filter efficiency (see fig. 4.2 d), and are also important to fully characterize any Josephson junction. Such measurements are performed using a sinusoidal waveform at low frequency (11.123 Hz) with an amplitude much smaller than the critical current of the sample as current bias, and reading the voltage across the junction using a lock in amplifier Stanford Research 530 with tunable sensitivity. The lock-in is used to achieve high precision ac measurements, because it attenuates to zero all the frequency components different from the reference signal, by integrating the input signal over an entire period of the reference signal.

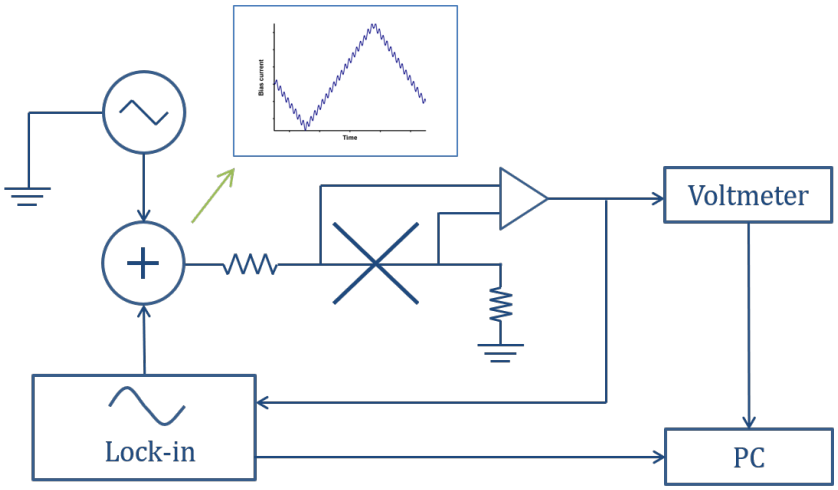

Figure 2.4: Scheme of the circuit used to measure dI/dV curves

Conductance spectra measurements allow to acquire information on density of states of the samples, as the differential conductance dI/dV versus V in a superconductor is proportional to the density of states[53]. In this case the input current is a sum of two signals: a low frequency (1 mHz) triangular ramp, and a small sinusoidal excitation at about 30 Hz. The optimal ratio between the two signal amplitudes is of the order of 10^{-3}. The output dV signal is read using the lock-in amplifier, while dI is given by the amplitude of the small sinusoidal excitation. The quasi-dc output voltage is read using an Agilent 34401A multimeter with a six digits display. The circuit scheme for such measurements is shown in fig. 2.4.

Besides the usual device characterization, a large part of this work is centered on testing ferromagnetic Josephson junctions as memory elements compatible for integration in superconducting digital SFQ circuits. Their use is based on the fact that MJJs can be switched between two states with different critical currents corresponding to logic '0' and '1' using magnetic field pulses. A significant result of this work is the analysis of the influence of RF fields on the switching processes of these devices.

Magnetic field pulses are generated using a two channels programmable pulse generator Keithley 3402, which allows the control of width, amplitude and other parameters such as delay, rising and falling time of the pulse. The voltage signal is sent to 1 kΩ shunt resistor and then to the superconducting coil. Since the coil is in the superconducting state during the measurements, the only resistance is provided by metallic contacts used for current biasing. This resistance is about 2 Ω, so the shunt resistance is much larger than the lines resistance and the coil is current biased. The RF train is emitted by

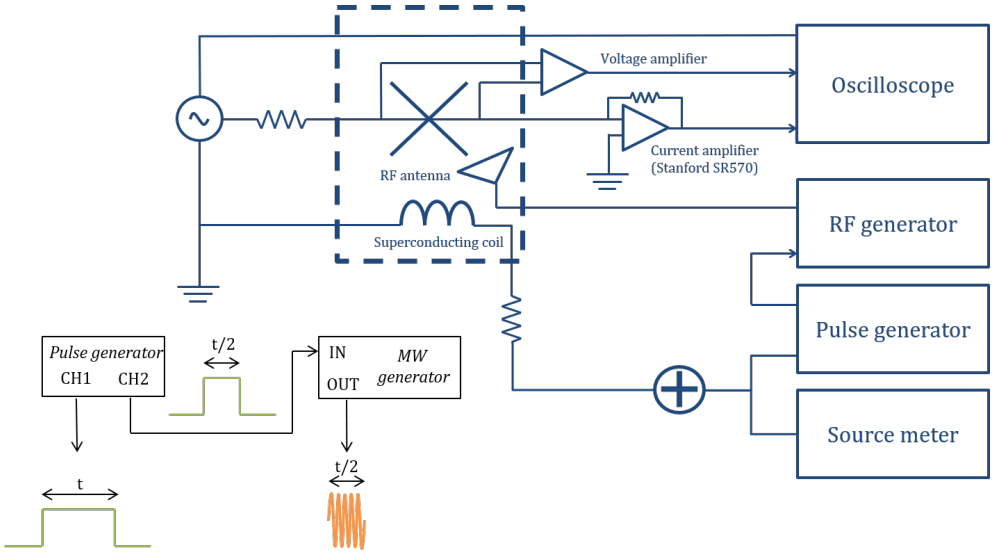

Figure 2.5: Scheme of the circuit used for memory testing

an antenna placed close to the sample and controlled through a microwave generator Rohde & Schwarz SWM 05 synchronized with the signal generator, so that it is possible to control its delay with respect to the magnetic field pulse and its length, as well as its frequency and power. Standard IV characteristics have been collected automatically after each pulse and then analyzed. The circuit scheme for such kind of measurements is shown in fig. 2.5.

In order to study the phase dynamics of a Josephson junctions, switching distribution measurements as a function of temperature and magnetic field are fundamental. The bias current is a triangular waveform ramped at a constant rate ($\sim$ 21 Hz) using an arbitrary waveform generator Agilent 33120A, with a dc offset to avoid switching to both positive and negative voltage: switching to the resistive state means heating of the sample, and a consequent change in the mean switching current and in the distribution width. Our electronic setup is sensitive to current variations of the order of few nA, so even a small heating of the sample can cause a systematic error in SCD measurements.

The output voltage is fed into a differential amplifier and then read by the oscilloscope. The current value is collected in a histogram when the voltage goes above a certain threshold value, chosen so that voltage noise in the superconducting branch is well below it. This avoids false switching events due to noise pick up (see fig.2.6). This setup is equivalent to the use of a threshold detector, which measures the junction voltage and sends a signal

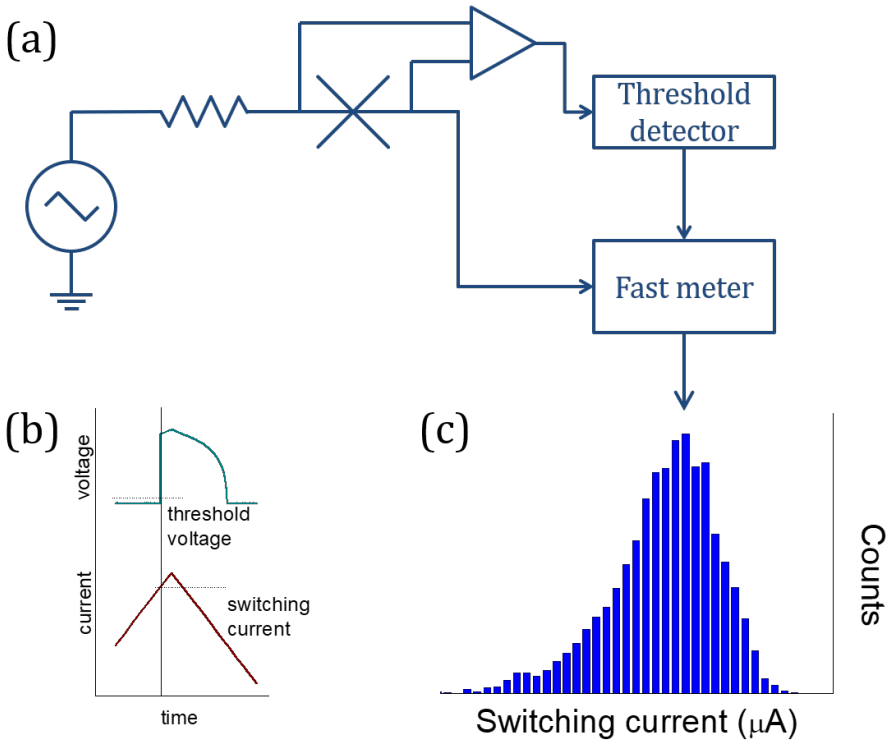

Figure 2.6: (a) Circuit scheme for SCD measurements. (b) junction output signals, and threshold voltage (black dashed line) set for SCD measurements. (c) switching current distribution histogram

to a fast meter that registers the corresponding current value.

At least 10^4 events are processed for each temperature and magnetic field value to fill the switching histogram. SCD measurements provide an estimation of the mean switching current (which can be used as an estimation of the critical current) with an error given by the distribution width. For our samples, the error is about 0.1%.

Chapter 3

Magnetic Josephson junctions for memory applications

3.1 State of the art

The new generation of large scale computing systems and data centers has an impressive power consumption: for each facility, it is of the order of hundreds of MW [54]. Cryogenic superconducting technology is an excellent candidate for the realization of the next generation of energy-efficient classical computing systems. Single Flux Quantum (SFQ) logic is based on the specific properties of superconductors, and it is sought to have applications also in quantum computing, with the realization of read-out, error-correction and control of qubit circuits.

However, the matching low power dissipation memory integrable in SFQ circuits is still missing. There have been several approaches to the problem, including hybrid memories [55] and the integration of spintronic memory elements [56, 57]. We choose to follow the approach that envisions the use of Josephson junctions with ferromagnetic barriers as memory elements[58, 59, 60, 61, 62, 63, 64]. To date, the use of these junctions as memory elements has been successfully demonstrated, but the overall memory cell, i.e. the memory element equipped with address and readout circuits, remains large. In this framework, it is crucial to develop new addressing approaches that can be employed in the design of memory cells of reduced size. Here we present a full chacterization of such SIsFS junctions as a function of temperature down to 0.3 K, and focus on the study of the effect of external RF fields on switching processes of magnetic Josephson junctions with high $I_C R_N$ product.

The RF-assisted magnetization switching is a rather well known phenomenon for a wide range of systems such as magnetic clusters, single-domain

magnetic particles and magnetic tunnel junctions [65, 66, 67, 68, 69, 70, 71, 72, 73], but it has never been investigated on MJJs. Here we show how this effect of remagnetization boost by RF fields can be used to improve discernibility of two logical states of a superconducting memory element based on $Pd_{0.99}Fe_{0.01}$ magnetic barrier.

3.2 Fabrication of SIsFS samples

Conventional SFS junctions have typical metallic properties such as low $I_C R_N$ (of the order of few μV), low capacitance and normal state resistance and overdamped phase dynamics, which results in a high dissipative behavior. In particular, the low $I_C R_N$ product and the high dissipation make them hardly compatible with standard SFQ logic, where the typical requirement is an $I_C R_N$ of the order of mV. The junctions used in this work have a high $I_C R_N$ product ($\approx 700\mu V$) when compared to standard SFS junctions, and low dissipation, compatible with standard SIS Josephson junctions used for superconducting circuits.

These junctions have been fabricated within a collaboration between HYPRES Inc. and ISSP[61]. They are characterized by a multilayer barrier, with a thin insulating layer (Al/AlO_x), a superconducting Nb layer with thickness of the order of the superconducting coherence length, and a soft ferromagnetic layer ($Pd_{0.99}$ $Fe_{0.01}$).

The first step is the fabrication of the bottom Nb-Al/AlO_x-Nb trilayer, using the standard HYPRES technology for 4.5 kA/cm^2 current density wafers [74, 75]. The Nb counter electrode has a thickness of 15 nm at this stage. The wafers are then diced into 15 mm x 15 mm samples and sent to ISSP, where the Nb counter electrode is etched down to $\sim$10 mm, in order to remove Nb oxide and possible organic residues on the surface, such providing a good interface for the deposition of the PdFe-Nb bilayer. The ferromagnetic layer is 14 - 18 nm thick for samples presented here, the junction mesa has a square shape of 10x10 μm^2. The thin Nb layer sandwiched between the oxide layer and the ferromagnet has a crucial role for the properties of these junctions. As pointed out in [76], for the thicknesses used for these devices, superconductivity is not completely suppressed, thus allowing the transmission of a sufficiently large supercurrent when compared to a SIFS junction. At the same time, since the thickness of the Niobium interlayer is smaller the London penetration depth, the multilayered barrier behaves as a single barrier in presence of magnetic field.

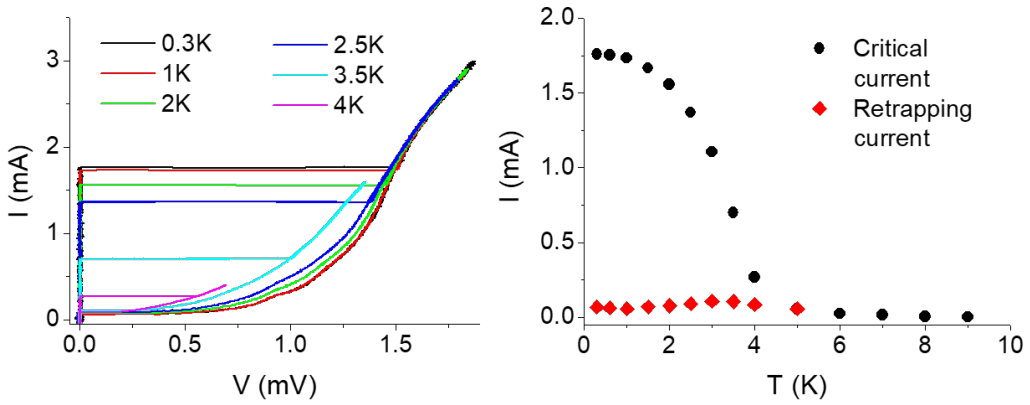

Figure 3.1: Left: IV curves as a function of temperature for a sample with PdFe layer thickness of 18 nm. Right: critical current and retrapping current for the same sample

3.3 IV curves and junction characterization

Ferromagnetic Josephson junctions exhibit different characteristics depending on the barrier. In order to put such samples in a wider framework, we measured IV curves as a function of temperature for a SIsFS junction with a 18 nm thick PdFe layer (fig.3.1). From the IV curves we obtain $I_C(T)$ curves with an Ambegaokar-Baratoff like behavior at low temperatures (from 0.3 K to 4 K) and a tail at higher temperatures characteristic of proximity effect [20] (fig.3.1). This behavior is consistent with the model reported in [76], where three different regimes for SIsFS junctions are described, depending on the thickness of the superconducting interlayer L_s. For $L_s \gg 3\xi_s$, where ξ_S is the coherence length of the superconductor, the device behaves as two Josephson junction in series, a standard tunnel junction and a metallic ferromagnetic junction. The overall properties are dominated by the junction with lower critical current, which is usually the SIs tunnel junction. The opposite case is $L_s \ll 3\xi_s$. In this case, superconductivity in the intermediate (s) layer is completely suppressed, and the device behaves as a standard SIFS junction[77].

Our samples fall in the intermediate case of junctions with an interlayer thickness $L_s \approx 3\xi_s$. In this case, the superconducting interlayer thickness is smaller than λ_L, and so the device behaves as a single junction in presence of external magnetic field. On the other hand, superconductivity is not completely suppressed within the superconducting interlayer, and so the critical current of the devices is high when compared to analogous SIFS junctions.

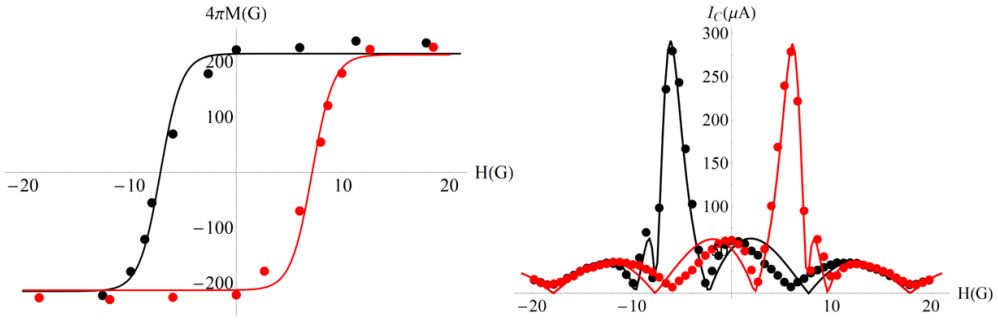

Figure 3.2: Experimental data and fitted curves for MJJ sample with $d_F = 14nm$.

In this thickness range, the properties of the junction are extremely sensitive to the thickness of the ferromagnetic layer and to the exchange field h. The latter tunes the effective transition temperature T_C^*, which is the transition temperature of the superconducting interlayer, causing the appearance of the proximity-like tail observed in fig.3.1.

The estimated quality factor for these junctions using the methods reported in [78] using IV curves is $Q = 40 \pm 8$. The normal state resistance R_N measured from IV curves is $\approx 6\Omega$, from eq.1.15 we obtain a capacitance $C = 8 \pm 3$ pF, which is a reasonable value for a tunnel junction.

The study of the junction parameters such as the quality factor, the capacitance and the resistance is a necessary step towards a complete characterization of such junctions towards their integration in complex circuits.

3.4 Application of Josephson magnetometry

The junctions analyzed in this chapter provide an excellent example of samples where the Josephson magnetometry protocol described in chapter 2 can be successfully applied. The magnetization curve is modeled by the phenomenological function

$$M(H) = \frac{2M_S}{1 + e^{-b(H+H_C)}} - M_S \tag{3.1}$$

and this function is then used to fit $I_C(H)$ experimental data using

$$I_C(H) = I_C^0 \left| \frac{\sin\left(\pi \frac{\Phi+\Phi_M}{\Phi_0}\right)}{\pi \frac{\Phi+\Phi_M}{\Phi_0}} \right| \tag{3.2}$$

The agreement between the experimental data and the fitted function is very good, the results of fitting procedure are shown in fig.3.2

3.5 Memory operation

The basic principles of operation for SIsFS junction are described in [61, 62]. The memory cell operation is based on the fact that for each magnetic field value there are two critical current values that can be used as two distinct logic states: $I_C(H)$ curves in ferromagnetic junctions are shifted and distorted depending on the sweeping direction of the magnetic field. When the external field goes from negative to positive values, the Fraunhofer pattern is shifted towards positive values of magnetic field, while it is shifted to negative H values when the field is ramped in the opposite direction. 'Read' operations are performed using a dc current I_R which is intermediate between the two critical current values that constitute the logic '0' and '1'. If I_R is larger than the critical current level, than the output signal is a finite voltage, while if I_R is smaller than the critical current level of the logic state then the output signal is zero voltage. 'Write' operations are performed using magnetic field pulses to switch between the two $I_C(H)$ curves.

3.6 Role of RF fields in switching processes

We use square field pulses 500 ms long, of different amplitudes, combined with RF pulses (see fig. 2.5) at fixed frequency of 3.88 GHz, chosen to ensure the maximum coupling with the junction. The optimal coupling condition is chosen by checking the reduction of critical current in presence of microwaves, and eventually the appearance of Shapiro steps (fig. 3.4 inset). This frequency is slightly higher than the ferromagnetic resonance (FMR) frequencies detected for 100 nm thick $Pd_{0.99}Fe_{0.01}$ layers [72], and provides effective magnetization dynamics due to microwaves. The exact optimal microwave frequency we use for this experiment depends only upon the geometry of our setup, i.e. the relative positions of the microwave antenna and the sample holder. This dependence is confirmed by a number of other experiments performed with the same setup not involving ferromagnetic materials performed using the same experimental setup. At other frequencies, the coupling between the antenna and the sample is strongly reduced. We observed that for frequencies different from the maximum coupling frequency, no effect on switching processes are observed (fig. 3.4). The RF train is modulated so that it is always centered around the center of the field pulse. For the

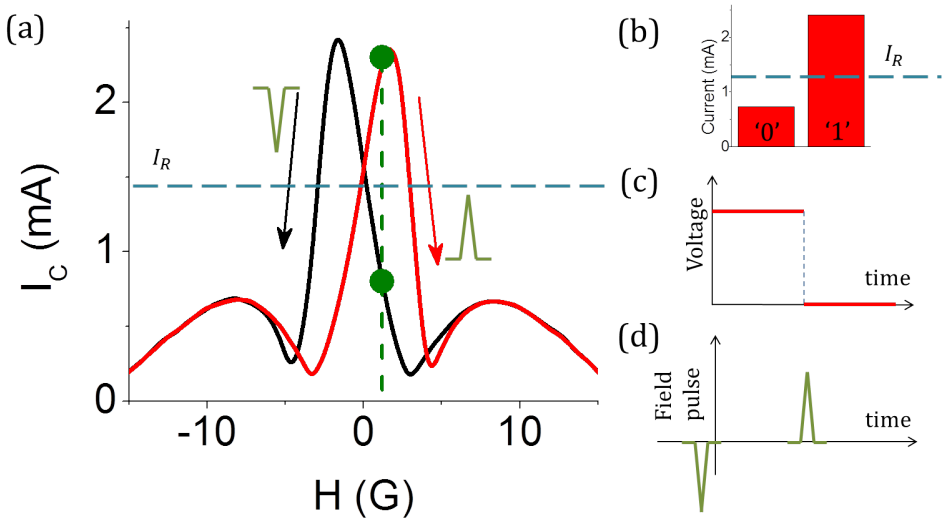

Figure 3.3: Functioning scheme of a MJJ memory element. (a) $I_C(H)$ curves. Black and red arrows indicate the sweeping direction of the magnetic field to obtain the corresponding curve, the magnetic field pulses used to switch are indicated in green close to the arrows. Green dots are the points corresponding to memory states. Blue horizontal line is the reading current I_r. (b) Critical current levels and the corresponding logical statese, blue line is the reading current. (c) Voltage levels corresponding to the two logical states. (d) Scheme of the pulses used to switch between logical states.

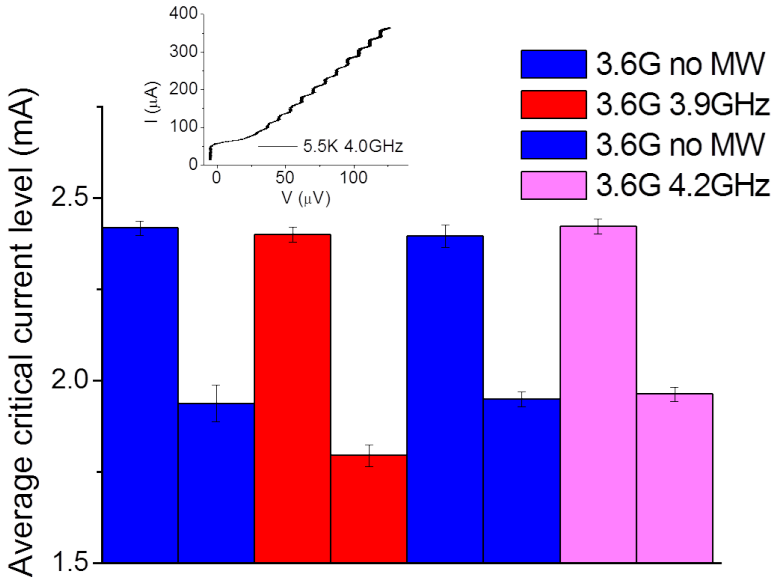

Figure 3.4: Critical current levels (average on 10 pairs of low-high current IV) for different microwave frequencies. Inset: appearance of Shapiro steps when the junction is efficiently coupled with microwaves

samples used in this work, the $I_C(H)$ curves obtained ramping the external field from negative to positive values and vice-versa are symmetrical with respect to zero field, so the memory cell use of this device requires a magnetic field bias to set the optimal working point. This corresponds to the magnetic field value for which the difference between the high and low critical current levels is as large as possible, provided that the magnetic field bias is within the saturation field. Taking all this into account, the chosen working point for all measurements presented here is 1.2 G.

The analysis is carried out by comparing the current levels obtained applying only magnetic field pulses and the current levels obtained applying microwaves together with field pulses respectively. In both cases critical current levels have been measured from standard IV curves acquired after the end of magnetic field pulse. The comparison has been performed collecting 10 pairs of low-high current IVs for each case, and ΔI in percentage is calculated from the average of low and high current levels as

$$\Delta I = \frac{I_C^{high} - I_C^{low}}{I_C^{high}} \times 100 \tag{3.3}$$

where I_C^{high} is the average of the high critical current levels and I_C^{low} is

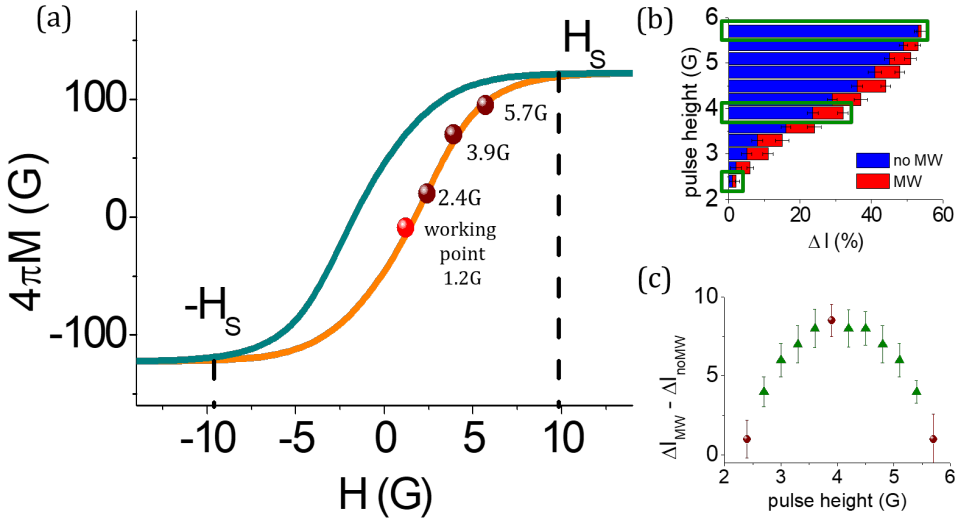

Figure 3.5: (a) $M(H)$ curve of the sample. The red dot is the chosen working point, brown dots indicate the pulse amplitudes framed by green squares in (b). (b) ΔI in absence (blue bars) and in presence (red bars) of microwaves, for different magnetic field pulse amplitudes. Green squares frame the pulse amplitudes indicated by brown dots in (a). (c) ΔI difference between the case with and without microwaves. The brown points correspond to the brown points in (a) and to the green frames in (b).

the average of the low critical current levels.

Uncertainty on ΔI is estimated by propagating the errors on the average high and low current levels:

$$err(\Delta I) = \Delta I \sqrt{\frac{err(I_C^{high})^2 + err(I_C^{low})^2}{(I_C^{high} - I_C^{low})^2} + \left(\frac{err(I_C^{high})}{I_C^{high}}\right)^2} \tag{3.4}$$

We observe an enhancement in the separation between current levels when RFs are applied for a wide range of field pulse amplitudes (fig. 3.5).

The enhancement increases with increasing field pulse amplitude up to a certain maximum, and then decreases again with a further increase of the field pulse amplitude. The minimum of this range is 2.4 G, which corresponds to $\approx 0.2 H_S$, the maximum is 5.7 G, which corresponds to $\approx 0.6 H_S$. Such values can be explained once taking into account the magnetization curve obtained using the methods described in Chapter 2. For small values of field pulses, very close to the working point, there is no difference between the case with and without microwaves, and in both cases ΔI is small ($\approx 2\%$). This can be

interpreted considering the field pulse as a small perturbation causing a linear response. For large amplitudes of the field pulses, $\Delta I \approx 55\%$ in both cases, due to the fact that with such field pulses we approach the saturation, where possible changes induced by external RF fields cannot be distinguished. The maximum enhancement is at 3.9 G, which is in an intermediate region of the $M(H)$ curve. In fig. 3.5c the difference between blue and red bars in fig. 3.5b is also plotted.

3.6.1 Energy dependence

In order to have a more detailed picture of the effect we measured the current level variations by changing the energy transfered to the sample. It is difficult to estimate the actual amount of energy transfered to the sample because of the setup used (fig. 2.5) : the RF emitting antenna is placed close to the sample, but the setup is not designed to accurately control the position. However, since this part of the experiment has been carried out all during the same cool down, we can assume the same emitting conditions for all cases and use the calculated emitted energy to discriminate different regimes. We perform the measurements changing the emitted energy in two ways: either we fix the power level and change only the duration, or we change both the power level and the time duration so that the product of the two is constant. We observe an enhancement in the separation between current levels increasing the emitted energy, as can be seen in fig. 3.6a, considering the average of the current levels calculated on 10 pairs of low-high IV pairs. Here, ΔI is the same within the error bars for same amounts of emitted energy, regardless of the power level and the time duration (fig. 3.6). The enhancement is even clearer if we consider fig. 3.6c and 3.6, where we show the current levels (non averaged) and ΔI fixing the power level and changing only the time duration of the RF train.

These experimental data point in the direction of an 'effective heating' of the barrier, since the RF effect increases with increasing energy emitted (and thus transfered heat). From a microscopic point of view, this effective heating can be interpreted as an RF-induced fluctuation of local magnetic moments in PdFe layer that decreases the coercive field and facilitates the remagnetization process, as already tested for other ferromagnetic systems[65, 66, 67, 68, 69, 70, 71, 72]. This hypothesis is confirmed by further measurements of the RF effect at different temperatures, as will be clearer in the following section.

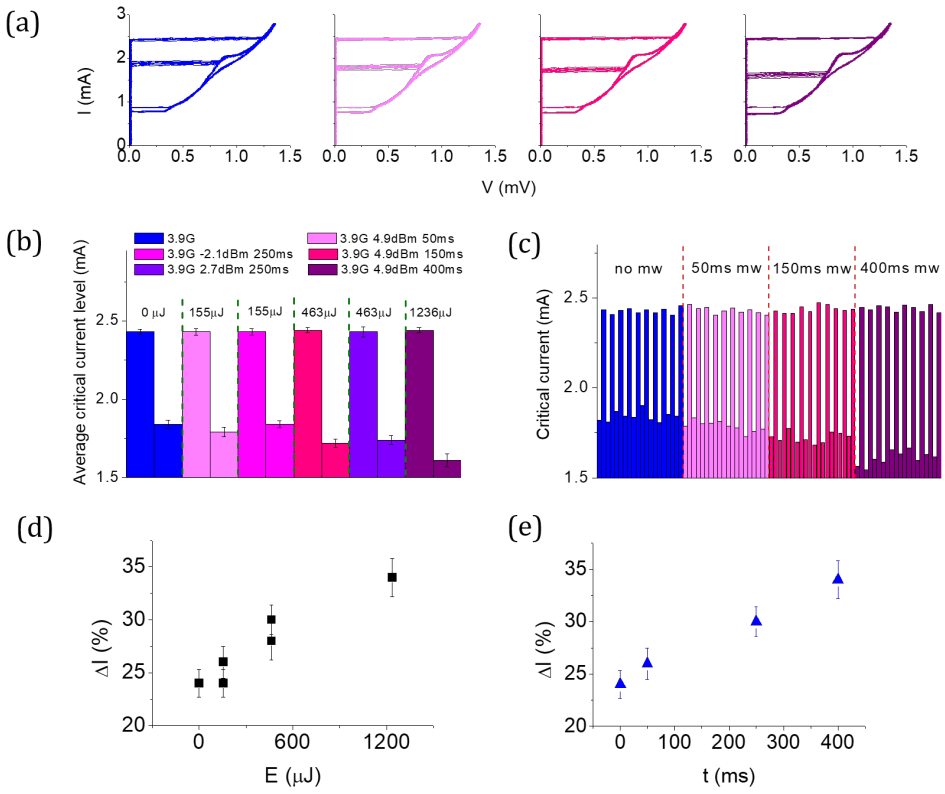

Figure 3.6: (a) IV curves for RF trains at 4.9 dBm and different time durations. From left to right: no microwaves, 50 ms, 150 ms, 250 ms, 400 ms. (b) Averaged high-low critical current levels for different emitted energies from the antenna. (c) Current levels for RF trains at 4.9 dBm ($\approx$ 3.1 mW) and different duration. (d) ΔI as a function of emitted energy. (e) ΔI as a function of the time duration of the pulse, fixed the power level.

3.6.2 Temperature dependence

Our measurements have also shown a temperature dependence of $\Delta I_{MW} - \Delta I_{noMW}$, i.e. the difference between the percentage current level separation in presence and in absence of external RF fields. We use magnetic field pulses with an amplitude of 3.9 G, combined with RF trains 250 ms long. The comparison with M(H) curves at different temperatures reveals a correspondence between the percentage difference in coercive field H_C and G defined as

$$G = \frac{\Delta I_{MW} - \Delta I_{noMW}}{\Delta I_{noMW}} \tag{3.5}$$

As seen in fig. 3.7a, the percentage variation G at a given temperature corresponds to the percentage variation of H_C between T and $T + \delta T$, where $\delta T \approx 0.5K$. In 3.7b and 3.7c we show the difference between the current levels in absence and in presence of microwaves at a certain temperature T and the corresponding M(H) curves at T and $T + \delta T$. The sudden change in M(H) curves seen in 3.7c has been recently explained taking into account a two-component magnetization of PdFe. It has been shown in [79] that thin ($<$ 20 nm) PdFe films with low iron content present two different Curie temperatures that correspond to two different interactions. The main contribution is due to short range interaction, while the weaker contribution is related to a Ruderman-Kittel-Kasuya-Yosida (RKKY) long range interaction. In our samples PdFe is 14 nm thick, with a higher Curie temperature T_{Curie_2} of about 12 K. According to Bol'ginov et al. [79], the lower Curie temperature T_{Curie_1} is around $0.4T_{Curie_2}$ for 20 nm PdFe thin films. In our case, $T_{Curie_1} \approx 4.8K$, which is in agreement with our observation of a sudden change in M(H) curves between 4.7 K and 5.0 K (fig. 3.8).

3.7 Limitations and perspectives

The development of SFQ-compatible Random Access Memories is constantly improving, following different approaches, such as MJJs but also hybrid semiconductor-superconductor devices, φ-junctions and spintronic memory elements [58, 59, 60, 61, 62].

In any case, the technological progress relies also on novel memory addressing schemes that can improve efficiency and scalability of such devices. Our experiment has several limits, but it demonstrates for the first time the use of RF fields as an additional knob to manipulate the memory state. In particular, the use of a RF emitting antenna limits our control of the microwave train, and cannot be considered as a viable approach for memory cell fabrication. At the same time, the large characteristic time ($\sim$ 2 ms)

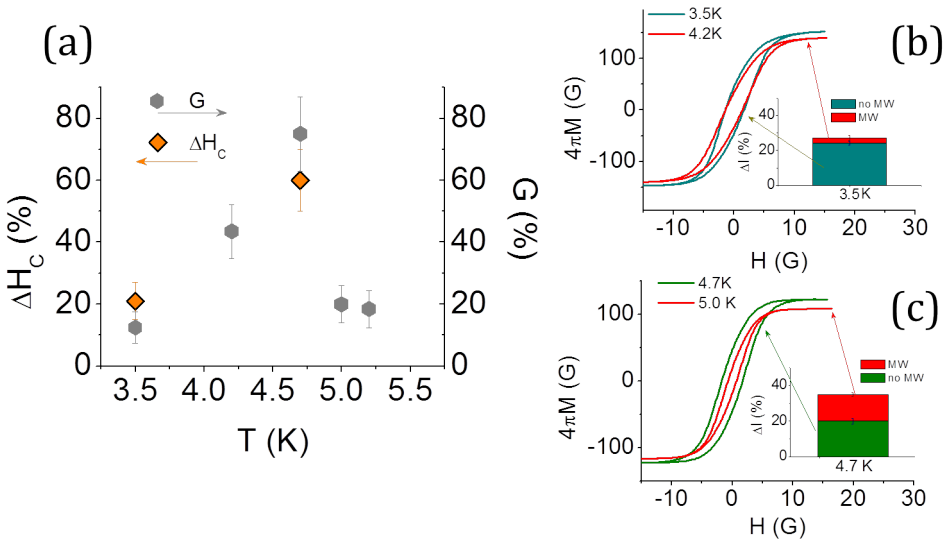

Figure 3.7: (a) Grey dots, scale on the right side: percentage enhancement of the current level separation with and without applied microwaves (G). Orange diamonds, scale on the left: percentage change in coercive field measured from M(H) at T and $T+\delta T$. (b) Magnetization curves at 3.5 K and 4.2 K. Inset: ΔI at 3.5 K. Blue: without applied microwaves, red: with applied microwaves. (c) Magnetization curves at 4.7 K and 5.0 K. Inset: ΔI at 4.7 K. Green: without applied microwaves, red: with applied microwaves. In (b) and (c) the arrows indicate the correspondence between M(H) and ΔI. It can be seen that the difference between ΔI_{MW} and ΔI_{noMW} corresponds to the difference between M(H) curves at different temperatures.

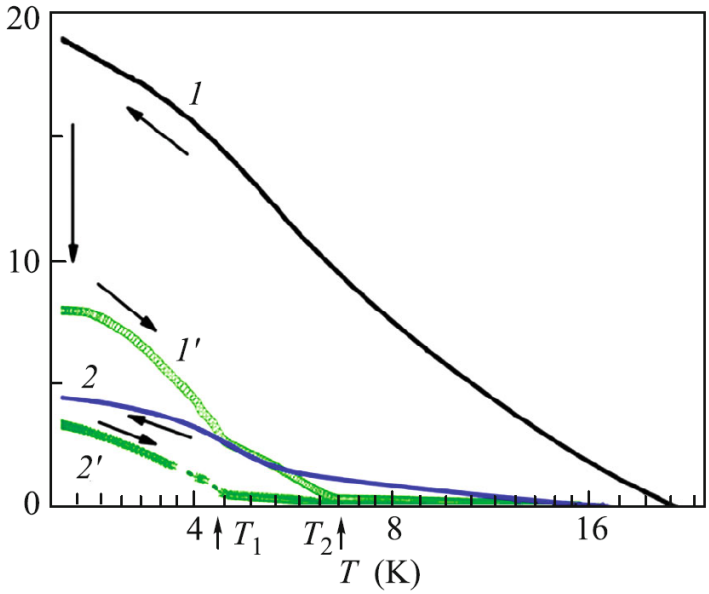

Figure 3.8: Figure from [79]. $M(T)$ curves for a 20 nm thick PdFe film measured on (1) cooling at $H = 40G$ and (2) at $H = 5G$, and curves measured when heating at $H = 0$ after cooling at (1') $H = 40G$ and (2') $H = 5G$

of the superconducting coil used to apply magnetic field pulses prevents us from observing the intrinsic switching times of MJJs.

To overcome the current limits, we plan an upgrade both of the setup and of the sample geometry, in order to use smaller samples with dedicate on-chip coplanar waveguides to apply microwaves.

Chapter 4

Spin Filters

In the last decade the interplay between competing order parameters at S/F interface has been extensively studied [21, 24], as well as the novel effects generated by a ferromagnetic barrier embedded in a Josephson junction [32, 40].

The NbN-GdN-NbN junctions measured in this work have a ferromagnetic insulator as a barrier. IV characteristics point to tunnel-like behavior, also confirmed by conductance spectra. This enriches the family of ferromagnetic junctions reported in literature where the ferromagnetic barrier has typically higher transparency and it is well described by conventional proximity effect. These junctions have a predominant second harmonic current-phase relation [80], and spin filtering properties [81]. These two features indicate the presence of the main ingredients for the formation of long range spin triplet supercurrents [24]: the spin filtering barrier provides the spin mixing that creates the triplet pairs with $S_Z = 0$, while the presence of a predominant second harmonic points to direction of higher order tunneling processes caused by a spin active interface that rotates the triplet pairs. In addition the observation of macroscopic quantum tunneling [9] demonstrates lower levels of dissipation when compared with the rest of junctions employing ferromagnetic barriers, thus making these devices excellent candidates for spintronic and quantum computation developments.

In the following, we will present a detailed investigation on the properties of samples with increasing spin filter efficiency, in order to point out the effect of spin mixing and spin rotation on the macroscopic parameters of different devices.

4.1 Fabrication

The junctions analyzed in this work have been fabricated at the Department of Materials Science and Metallurgy of University of Cambridge from NbN-GdN-NbN trilayers grown on oxidized Si substrated precoated with a 10 mn thick MgO buffer layer, using d.c. reactive magnetron sputtering in a Ar/N_2 atmosphere from pure Nb and Gd targets. GdN thickness was controlled by changing the deposition rate for each substrate within the same deposition run, using a computer-controlled stepper-motor in order to rotate different substrates at different speeds below a stationary Gd target[80, 82].

This procedure ensures that all samples in the same fabrication run are grown in the same conditions, and at the same time each sample has a different barrier thickness, due to the different rotation speed. The main error source on the barrier thickness values is a systematic error which is equal for all samples. This type of error does not affect our final results.

The growth conditions are fundamental to determine the final properties of the devices [82]. In particular, nitrogen vacancies can cause the appearance of a secondary phase of GdN (GdN-II), which is antiferromagnetic, and an increase in T_{Curie} above 60 K.

The junctions have a square mesa geometry defined by optical lithography and selective reactive etching of top NbN layer in CF_4 plasma. The NbN bottom layer in $\approx 100nm$ thick and acts as bottom contact, while the top contact is achieved by depositing a thin Nb wiring layer on top NbN electrode, which is $\approx 100nm$ thick.

4.2 Spin filter efficiency

The fingerprint of spin filter Josephson junctions is the R(T) curve, which is characteristic of this kind of junctions and allows the indirect measurement of spin filter efficiency (SFE)[81]. SFE measures the difference in conductivity for spin up and spin down channels due to the exchange splitting induced by GdN barrier, and is defined as

$$P = \frac{|\sigma_\uparrow - \sigma_\downarrow|}{\sigma_\uparrow + \sigma_\downarrow} \tag{4.1}$$

where $\sigma_{\uparrow(\downarrow)}$ is the conductance for spin up and spin down electrons. The tunnel conductance σ depends on the barrier height [83], so below the Curie temperature of GdN thin film ($T_{Curie} \approx 35K$), where the barrier height is different for spin up and spin down, the tunneling current is spin-polarized.

At high temperatures the resistance versus temperature curves shows a typical exponential semiconducting behavior, as commonly observed in Josephson junctions with NbN electrodes. Below T_{Curie}, the resistance starts to decrease with decreasing temperature, due to the activation of the exchange splitting of the ferromagnet. In this case, the two spin channels see two different barrier heights, as in one case the exchange field h is added to the barrier energy E_0 and for the other spin channel it is subtracted (fig.4.1, inset). An approximate expression for tunnel conductance is given by

$$\sigma \approx \sqrt{E} \exp -\frac{2d\sqrt{2mE}}{\hbar} \tag{4.2}$$

where E is the barrier height and d is the thickness of GdN barrier. For small exchange field h, when substituted into 4.1, this equation leads to

$$P \approx \tanh\left(\cosh^{-1}\left(\frac{R^*}{R}\right)\right) \tag{4.3}$$

where R is the measured value for the resistance and R^* is the extrapolated resistance value in absence of exchange splitting. Operatively, R^* is estimated by fitting the exponential branch of $R(T)$ above T_{Curie} using a standard semiconducting model[84]

$$R(T) = A \exp \frac{B}{T + T_0} \tag{4.4}$$

where A, B and T_0 are phenomenological parameters.

We measured NbN-GdN-NbN Josephson junctions with barrier thicknesses ranging from 1.5 nm to 4 nm. The spin filter efficiency increases with increasing thickness, and saturates at large thicknesses, as can be seen from fig. 4.2d. SFE values have large error bars due to the estimation procedure, but the relation between barrier thickness and spin filter efficiency is unambiguous[81]. Thus the characterization of the samples as a function of thickness provides a reliable method to study the properties of this kind of junction as a function of spin filter efficiency. Resistance versus temperature curves for different thicknesses show an increasingly pronounced peak as the thickness increases, while the Curie temperature, defined as the temperature where the resistance R is maximum, is almost constant. The room temperature resistance increases exponentially as expected for samples where tunnel conductance is predominant. According to [83], the tunneling resistance is given by

$$R(t, E_0) = \frac{2}{3\sqrt{2meE_0}} \left(\frac{h}{e}\right)^2 2\sqrt{\frac{2me}{\hbar^2}} t \exp \frac{4\pi t}{h} \sqrt{2meE_0} \tag{4.5}$$

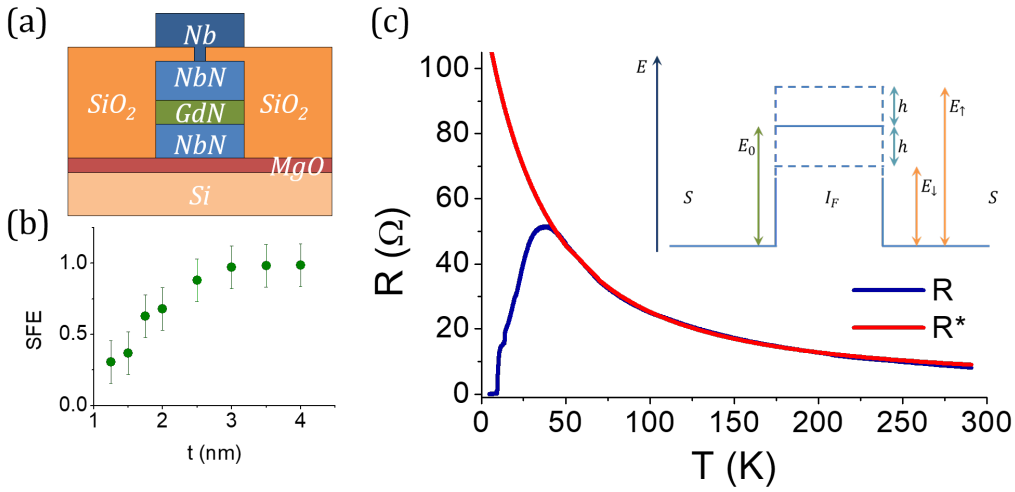

Figure 4.1: (a) Schematic cross section of a junction. (b) Spin filter efficiency as a function of barrier thickness (c) R(T) curve for a sample with high spin filter efficiency. Inset: barrier height for different spin channels. Above the Curie temperature T_{Curie}, both spin up and spin down electrons see the same barrier height E_0, and the R(T) curve (blue line) has the typical semiconducting behavior of NbN JJs. When the junction is cooled below T_{Curie}, the two spin channels see different barrier heights. In particular, one of the spin channels sees a barrier height $E_\downarrow < E_0$. The lowering of the barrier causes the resistance decrease measured in R(T) curves below T_{Curie}. The red line R^* represents the resistance extrapolated in absence of exchange field.

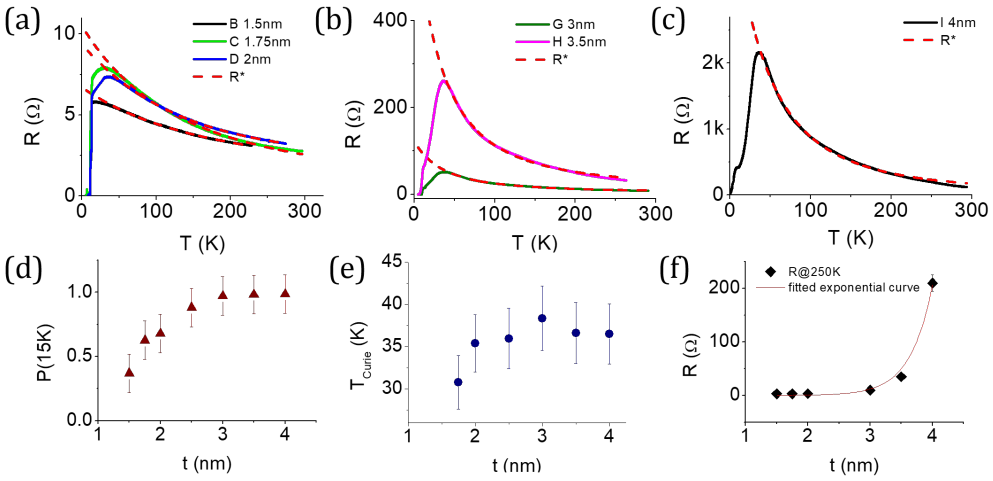

Figure 4.2: (a), (b) and (c) R(T) curves for different spin filter samples. Red lines indicate the extrapolated resistance in absence of exchange field. As the barrier thickness increases, the R(T) peak becomes more pronounced and the peak resistance increases. (d) Spin filter efficiency as a function of thickness calculated from R(T). (e) Curie temperature as a function of thickness, measured from R(T) curves. No Curie temperature is indicated for 1.5 nm sample, as for this thickness the barrier is not ferromagnetic, at least above the superconducting transition temperature. (f) Room temperature resistance as a function of thickness. Values are well fitted using a simple exponential model [83] (red line).

where m and e are respectively the electron mass and charge, t is the barrier thickness and E_0 is the energy height of the barrier. Assuming E_0 constant for all samples, it is possible to estimate it by fitting eq. 4.5 to experimental data. We estimate $E_0 = 0.36 \pm 0.12V$ (fig. 4.2f).

4.3 IV curves versus thickness

Current-voltage characteristics are a fundamental tool to investigate the properties of Josephson junctions, and in the case of spin filter junctions, different thicknesses correspond to different spin filter efficiencies. In order to point out the effect of spin filtering properties on the overall behavior of the junctions we measure I-V characteristics as a function of thickness.

As we have seen in chapter 1, from IV curves it is possible to determine some characteristic parameters such as the critical current I_C, the switching voltage V_S and the normal state resistance R_N, but also the dissipation regime

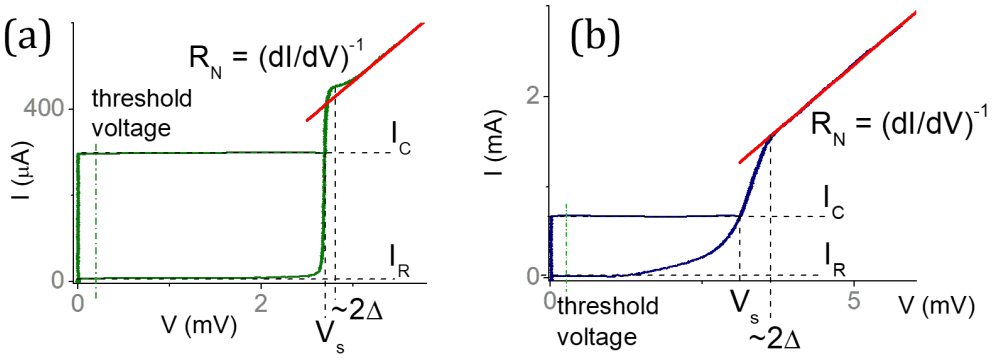

Figure 4.3: IV characteristic at 0.3 K for (a) a standard Nb-Al/AlO_x-Nb tunnel junction, (b) a sample with 1.5 nm thick barrier (SFE $< 30\%$), with labels indicating the characteristic parameters: critical current (I_C), retrapping current (I_R), switching voltage (V_{switch}), superconducting gap (2Δ) and normal state resistance (R_N). In the second junction is clearly visible a suppression of the switching voltage with respect to conventional junctions.

of the junction. The critical current is defined as the maximum supercurrent value, after which the junction switches into the resistive state. Operatively, for hysteretic Josephson junctions, we define I_C as the current at a certain threshold voltage, typically 10 μV - 100 μV. The switching voltage is the finite voltage on the subgap branch corresponding to I_C. The retrapping current is defined as the current at which the junction switches back to the non-resistive branch. We take I_R as the minimum current at the same threshold voltage used for I_C. The normal state resistance R_N is estimated from the slope of the linear fit of the IV region above the superconducting gap (fig.4.3).

We analyzed IV curves at 0.3 K for junctions with different barrier thicknesses, and extracted their characteristic parameters. Critical currents range from 30 nA for 4 nm junctions to 800 μA for 1.5 nm sample, and the corresponding current density ranges from $0.6 \times 10^{-2} A/cm^2$ to $16 \times 10^2 A/cm^2$. When compared with IV curves for standard tunnel junctions (see fig.4.3), it is possible to notice a strong suppression of the critical current, so that the corresponding switching voltage is well below the superconducting gap and decreases with increasing thickness, which for standard tunnel junctions also corresponds to $\approx I_C R_N$ product. For these junctions, R_N is obtained from a linear fit of the IV curves above the superconducting gap, as in fig. 4.3.

It is well known that in metallic, diffusive S/F/S, where the supercurrent is mainly due to proximity effect, $I_C R_N$ product decays exponentially with increasing thickness [85, 86, 87, 88, 89] , and it has been shown that in certain

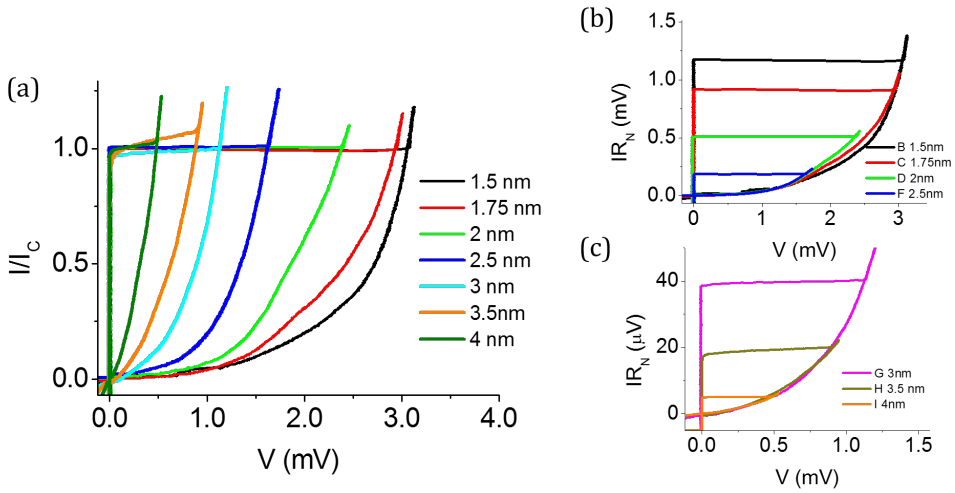

Figure 4.4: IV curves at 0.3 K for samples with different barrier thicknesses. In order to compare them it is necessary to normalize them with respect to some characteristic parameters, since the critical current and the switching voltage vary in a range of several orders of magnitude. (a) IV curves normalized with respect to the critical current: it is easy to see the suppression of switching voltage with increasing thickness. (b) and (c) IV curves normalized with respect to R_N: (b) barrier thicknesses from 1.5 nm to 2.5 nm, (c) barrier thicknesses from 3 nm to 4nm.

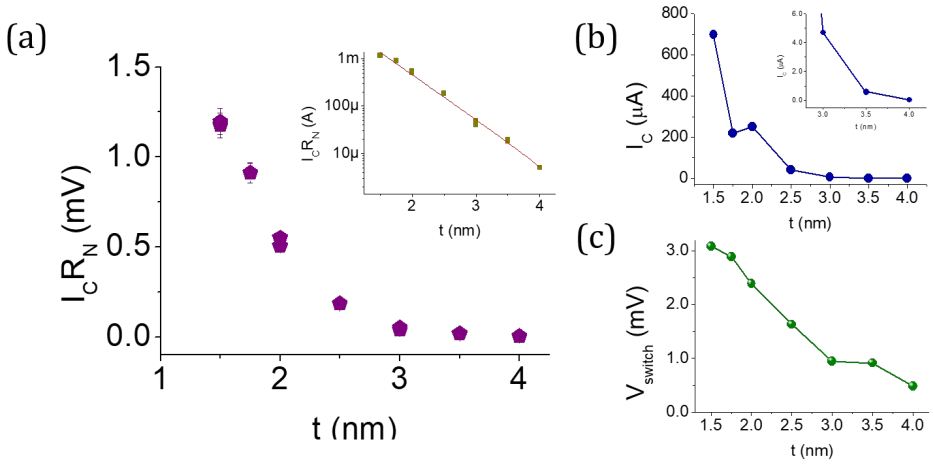

Figure 4.5: (a) $I_C R_N$ product as a function of thickness. Inset: $I_C R_N$ in log scale, and exponential fit of the data (red line). (b) Critical current as a function of thickness. (c) Switching voltage as a function of thickness.

cases $I_C R_N(d)$ can be fitted using a simple exponential decay, with a decay constant given by the mean free path in F layer [90]. The result of data fitting with an exponential curve of the type $y = A \exp(-x/\xi)$[85, 86, 87] is shown in fig.4.5, where the fitted decay length is ≈ 0.6 nm, while the room temperature mean free path of GdN reported in literature is 11 nm [91]. The failure of such well-known model for diffusive junctions points in the direction of a tunnel transport mechanism.

In fig. 4.4 a, IV curves are normalized with respect to the critical current to highlight the consequent reduction of the switching voltage, and the apparent linearization of the quasiparticle branch. In fig. 4.4 b and c, the normalization with respect to normal state resistance shows that all the junction have roughly the same subgap branch, which is typical of underdamped junctions with quality factors $Q \sim 10$, and and an increasing critical current suppression, due to increasing spin filter efficiency. The standard methods to evaluate the quality factor from the ratio I_C/I_R, as described in [78, 92, 93] cannot thus be used, especially on junctions with high SFE, as the models refer to conventional tunnel junctions where critical current is not suppressed due to spin polarization.

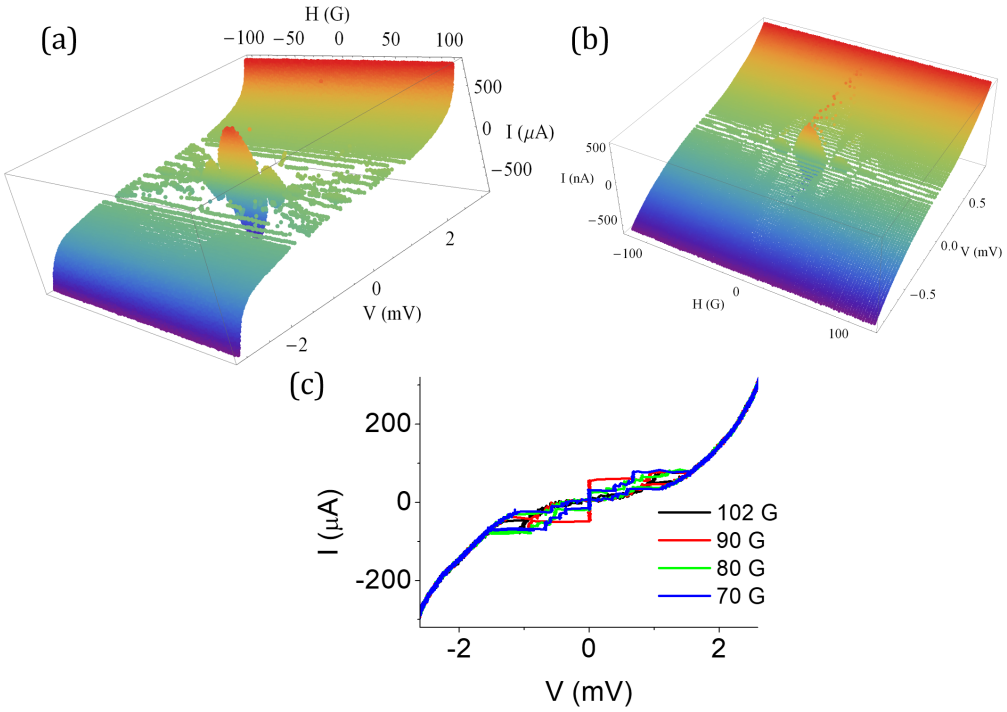

Figure 4.6: IV curves at 0.3 K as a function of magnetic field for junction with (a) 1.5 nm barrier, (b) junction with 3.5 nm barrier. (c) IV curves at high fields for the junction with thinner barrier. Magnetic field resonances can be seen in the subgap region.

4.4 IV curves as a function of external magnetic field

In order to fully characterize a Josephson junction, the behavior in external magnetic field is crucial. The measurements presented here have been performed as described in chapter 2, using a current biased superconducting coil to generate uniform magnetic field and collecting IV curves with an oscilloscope. Collecting IV curves at different magnetic fields enables us to analyze the critical current behavior and the subgap branches simultaneously. We are also able to see effects in the Fraunhofer pattern due to current asymmetries. In fig. 4.6 we show the 3D plot of IV curves at 0.3 K as a function of magnetic field for two different junctions, one with 1.5 nm thick barrier (non spin filter), and the other with 3.5 nm thick barrier (high spin filter efficiency). The second junction shows a subgap structure with no resonances. In fig.

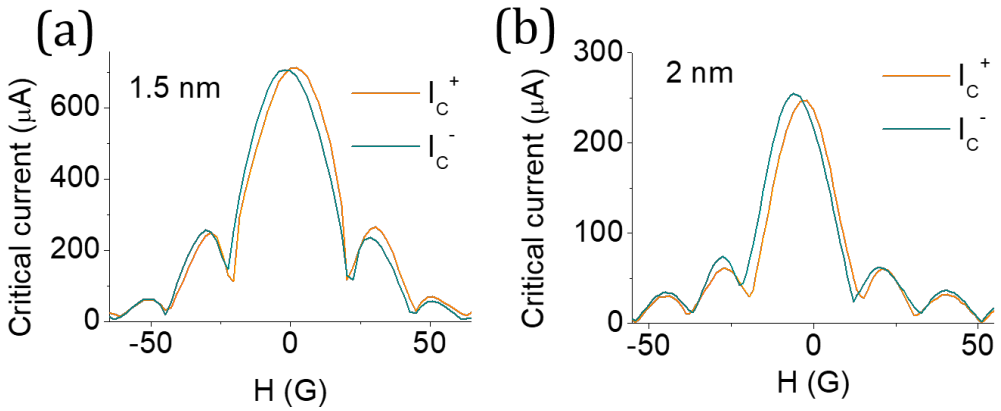

Figure 4.7: Critical current asymmetry for (a) sample with 1.5 nm thick barrier, with $L/\lambda_J \approx 1.5$, and (b) sample with 2 nm thick barrier, with $L/\lambda_J \approx 1$

4.8 we show $I_C(H)$ curves for samples with barrier thicknesses ranging from 1.5 nm to 4 nm. All the junctions fall in the short junction limit [3], except the 1.5 nm barrier thick sample, which presents a weak asymmetry between I_C^+ and I_C^-, which is in agreement with the calculated ratio $L/\lambda_J \approx 1.5$ and the 2 nm barrier thick sample, which lies at the boundary between the two regimes, with a ratio $L/\lambda_J \approx 1$, where λ_J is calculated using eq. 1.6 and eq. 1.8 (see fig.4.7).

It has been demonstrated [80] that for high spin filter efficiencies, i.e. thick barriers, the current-phase relation is a pure second harmonic. However, a systematic study on intermediate junctions has never been performed. In the following, we analyze $I_C(H)$ curves for different barrier thicknesses, using the model for junctions with a second harmonic component in the current-phase relation provided by Goldobin et al.[36]. In the following, we will review briefly the model and apply it to our samples.

4.4.1 Second harmonic current phase-relation

As we reported in chapter 1, the first Josephson equation provides a relation between current and phase of the type

$$j_s = j_c \sin\varphi \tag{4.6}$$

The presence of a ferromagnetic barrier can cause a strongly non-sinusoidal current-phase relation, and modify eq. 4.6 into

$$j_s = j_{c1} \sin\varphi + j_{c2} \sin 2\varphi = j_{c1} \left(\sin\varphi + g \sin 2\varphi\right) \tag{4.7}$$

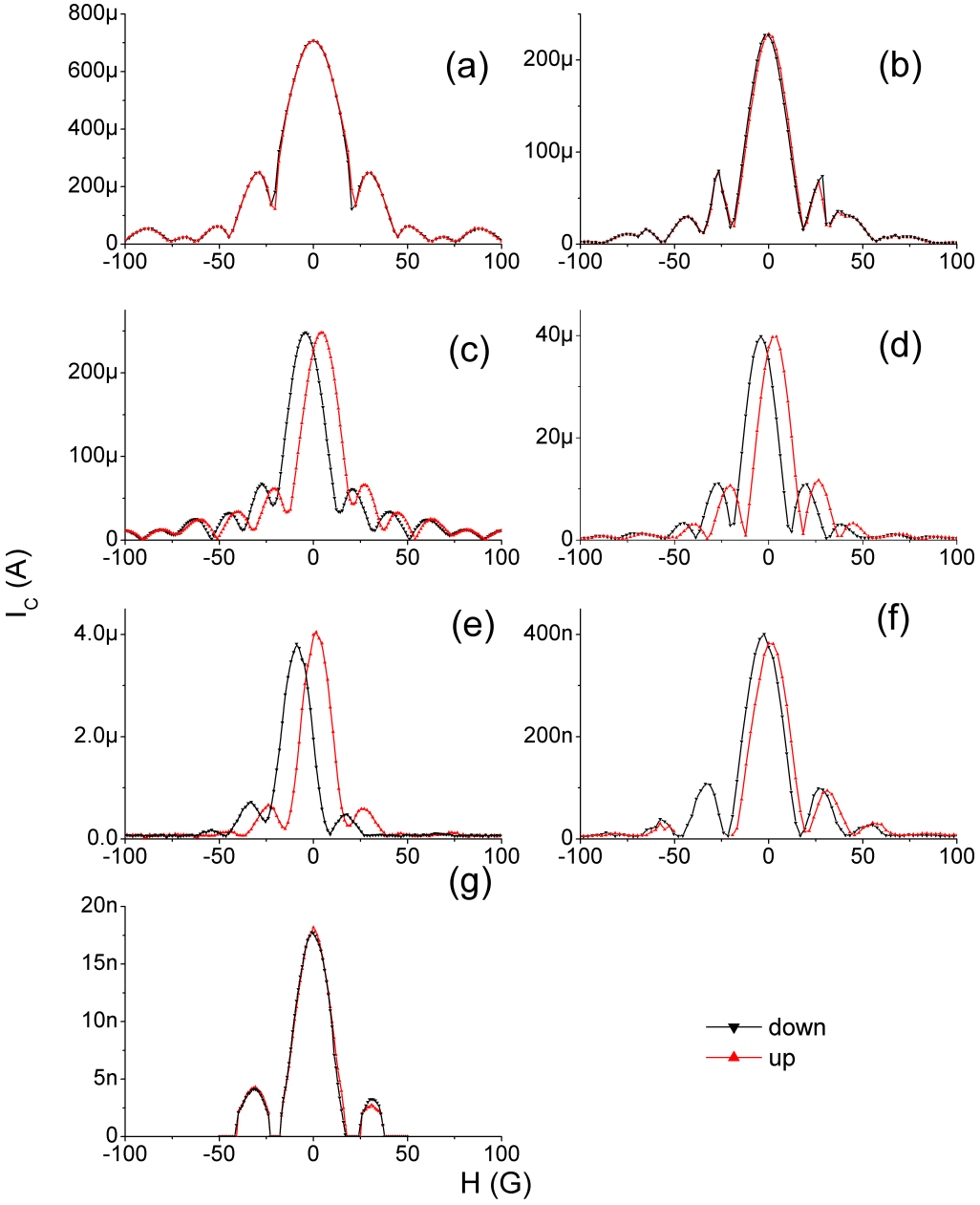

Figure 4.8: $I_C(H)$ curves for junctions with different barrier thicknesses. (a) 1.5 nm, (b) 1.75 nm, (c) 2 nm, (d) 2.5 nm, (e) 3 nm, (f) 3.5 nm, (g) 4 nm. Red curves are obtained sweeping the magnetic field from negative to positive values, while black curves are obtained sweeping the field from positive to negative values

where $g = \frac{j_{c2}}{j_{c1}}$. Calculating $I_C(H)$ dependence in the usual way for a short junction[3] using eq. 4.7 yields [36]:

$$I_C(H) = j_{c1} LW \left| \frac{2\sin\left(\frac{\pi\Lambda LH}{\Phi_0}\right)\sin(\phi_\pm) + g\sin\left(\frac{2\pi\Lambda LH}{\Phi_0}\right)\sin(2\phi_\pm)}{2\frac{\pi\Lambda HL}{\Phi_0}} \right| \tag{4.8}$$

where $\Lambda = \frac{\Phi_0}{H_0 L}$, L and W are length and width of the junction respectively, and Φ_0 is the single flux quantum. H_0 is defined by $H_0 A = \Phi_0$, where A is the effective area of the junction. The phase $\varphi_\pm$ can assume two values, which are obtained by the maximization of the supercurrent $I_S(\varphi, H)$ with respect to φ:

$$\cos(\varphi_+) = \frac{-1 + \sqrt{1 + 32g^2\cos^2\left(\frac{\pi\Lambda LH}{\Phi_0}\right)}}{8g\cos(\frac{\pi\Lambda HL}{\Phi_0})} \tag{4.9}$$

$$\cos(\varphi_-) = \frac{-1 - \sqrt{1 + 32g^2\cos^2\left(\frac{\pi\Lambda LH}{\Phi_0}\right)}}{8g\cos(\frac{\pi\Lambda HL}{\Phi_0})} \tag{4.10}$$

It should be not that in case of a single harmonic in the current phase relation, the phase value maximizing $I_C(H)$ is only one. It is useful to define from now on

$$I_C^+(H) = I_C(\varphi_+, H) \tag{4.11}$$

$$I_C^-(H) = I_C(\varphi_-, H) \tag{4.12}$$

Since $|\cos\phi_-| < 1$ only for |g|>1/2, and in this case, the condition is satisfied only for certain values of the magnetic field H, and so I_C^- is defined only for such values of the magnetic field. In fig. 4.9, the two expressions for the critical current are plotted for $g = 3$, and the regions where $I_C^-(H)$ is not defined are the sharp peaks in the green curve. The two functions are both normalized to I_C^+ maximum.

The lower critical current can be seen in a deterministic fashion only under given conditions of damping and temperature, using an appropriate current ramp (see fig.4.9 right) [37]. We tested our samples using different current ramps in order to be able to measure I_C^- where possible, but we always observed a single critical current. This, together with the observation that experimental Fraunhofer pattern show no discontinuities for any value of the magnetic field, led us to the assumption that eq. 4.9 should be used

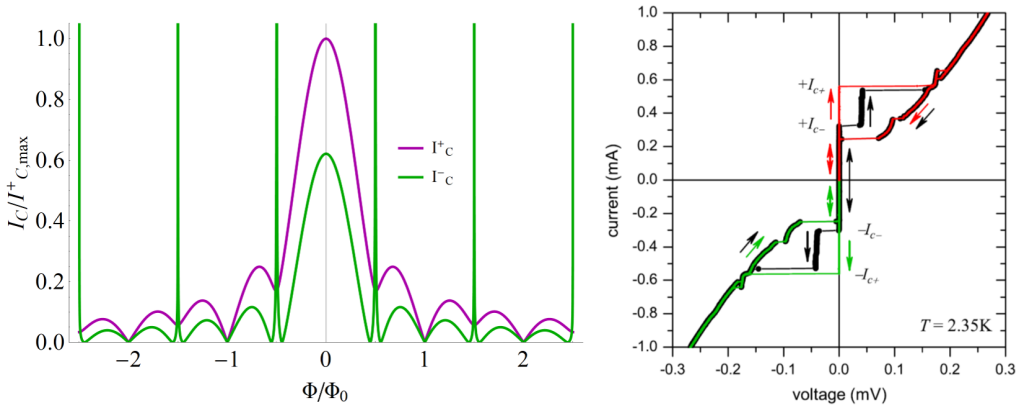

Figure 4.9: Left: I_C^+ and I_C^- calculated using the equations obtained in [36]. The sharp peaks of I_C^- indicate the regions where the function is not defined. Right: IV characteristic of a φ-junction showing two distinct critical currents. I_{C-} is obtained ramping the current from negative to positive values and viceversa. $\pm I_{C+}$ observation corresponds to positive (negative) current ramp. From [37].

for the fitting procedure. In fig.4.10 we show experimental data and fitted curves for samples with 1.5 nm and 2 nm thick barriers. For the thinner sample, the model works reasonably well up to the first secondary lobe. For the other sample, there is a clear indication of the fact that also effects due to barrier magnetization should be taken into account for a complete modeling. In fig. 4.10 (b) and (c) we show $I_C(H)$ curves obtained ramping the magnetic field from positive to negative values and viceversa. The fitted curves are in agreement with experimental data from negative fields up to the first positive lobe for fig (b) and from the first negative secondary lobe up to positive fields for fig. (c). These regions correspond to the regions of the magnetization curves where M does not depend on the external field H, and so its contribution is reduced to a simple shift along the x axis, which can be easily accounted for. A more detailed description of M(H) curves could allow a better fitting also of the other regions. In chapter 1 and chapter 3 we showed how magnetization curves for ferromagnetic barriers can be extrapolated for $I_C(H)$ curves. This procedure does not give an accurate description of M(H) curves when the samples are not fully magnetized, i.e. the applied fields are lower than the saturation field for the given ferromagnetic barrier. In this case, this procedure is not applicable, as the saturation fields for these samples are much larger than the applied fields. Nevertheless, the estimation of the second harmonic contribution for these samples is consistent with the

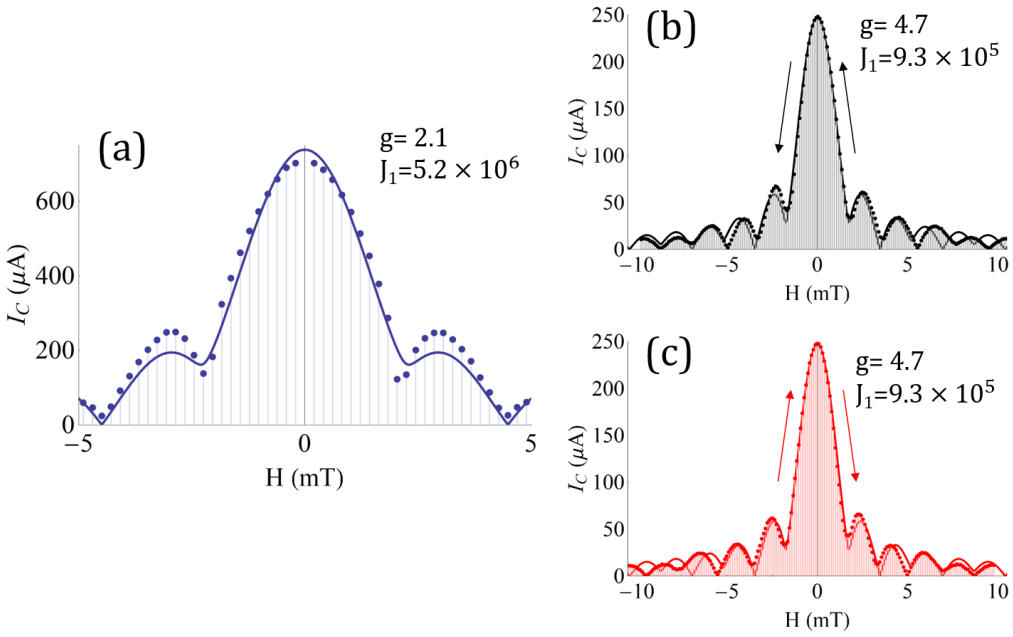

Figure 4.10: Experimental data and fitted curves using eq. 4.8 for samples with different barrier thicknesses. (a) 1.5 nm (b) 2 nm, with magnetic field ramped from positive to negative values, (c) 2 nm with magnetic field ramped from negative to positive values. Experimental data in (b) and (c) have been shifted to set $I_C(H)$ maximum at zero field.

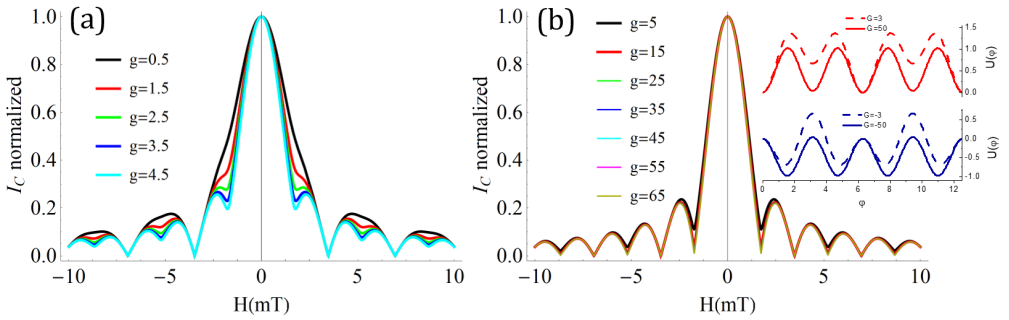

Figure 4.11: Simulated curves for different second harmonic contributions g. (a) Fraunhofer patterns for g between 0.5 and 4.5. (b) Fraunhofer patterns for high g (between 5 and 65). Inset: washboard potential in presence of second harmonic component.

other parameters such critical current density J_C and spin filter efficiency SFE.

For samples with thick barriers and high spin filter efficiencies as the ones shown in fig. 4.12, the model fails to give an estimate of the second harmonic contribution. This is due to the fact that for g above 10, it is not possible to discriminate $I_C(H)$ curves for different g values (see fig. 4.11), and eventually the outcome is equivalent to the one obtained using a pure second harmonic current-phase relation:

$$I_C(H) = I_{C_0} \left| \frac{\sin\left(\frac{2\pi\Phi}{\Phi_0}\right)}{\frac{2\pi\Phi}{\Phi_0}} \right| \tag{4.13}$$

We have shown that the model reported in literature [36] gives a reasonable description of our experimental data, and allows us to estimate the second harmonic contribution for different spin filter efficiencies.

It is well known that in conventional ferromagnetic junctions, where the exchange field is uniform, a dominant second harmonic in the current phase relation might appear only in the vicinity of 0-π transition[36, 21, 35]. On the other hand, it has been reported[80] for spin filter junctions with high spin filter efficiency a robust, pure second harmonic current-phase relation.

It has been predicted that in long, ballistic SFS junctions a predominant second harmonic in the current-phase relation, insensitive to temperature and impurities, appears when the junction has only one spin active interface[94]. This current-phase relation is directly related to higher order tunneling processes involving two Cooper pairs at a time. Such higher order terms would be

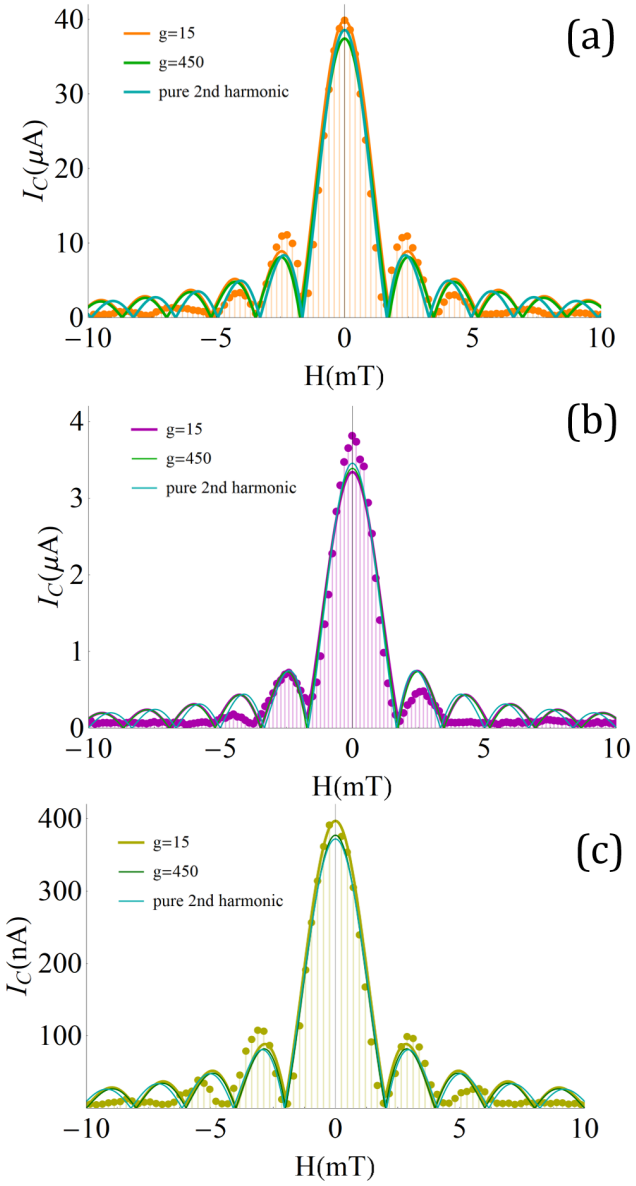

Figure 4.12: Experimental data and fitted curves for samples with thick barrier and high spin filter efficiency. (a) 2.5 nm barrier, (b) 3 nm barrier, (c) 3.5 nm barrier. In all cases, different but sufficiently high values of g ($>$10) produce good fits, as well as pure second harmonic fitting function (eq. 4.13)

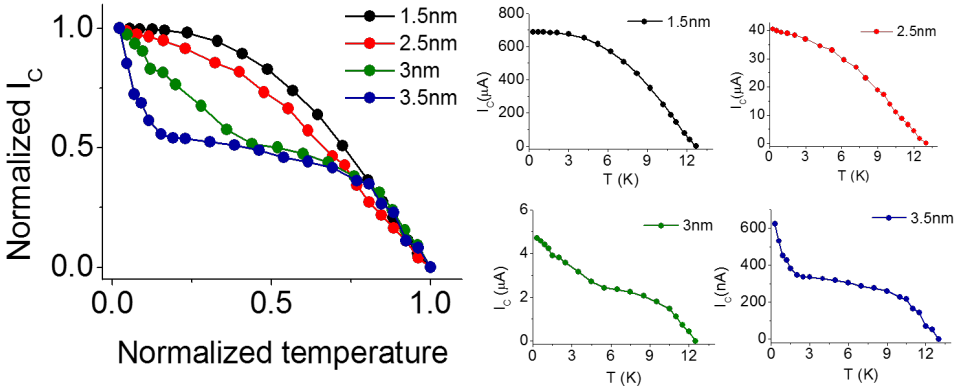

Figure 4.13: Critical current versus temperature for different barrier thicknesses. Left: normalized curves. Right: non normalized curves for each sample

consistent with a long-range triplet supercurrent[94], and this picture could fit our experimental results.

4.5 Critical current versus temperature

It should be noted that the Fraunhofer pattern alone cannot be used as proof of unconventional transport mechanisms, as $I_C(H)$ curves can be affected by a number of factors, such as barrier magnetization or inhomogeineities, which cause shifts and distortion of the Fraunhofer pattern.

Our measurements on spin filter junctions have demonstrated for the first time an anomalous $I_C(T)$ behavior for samples with thicker barriers (3 nm, 3.5 nm and 4 nm), enforcing the suggestion that non conventional transport mechanisms play a major role in these junctions.

In junctions with thin barriers (1.5 nm), $I_C(T)$ curves show a standard Ambegaokar-Baratoff (AB) behavior, with a saturation at low temperature. However, in order to fit the data with using AB relation, it is necessary to add a normalization factor to take into account the current suppression due to spin filtering. In our case, $r = 0.5 \pm 0.1$. As the barrier thickness increases, it is possible to notice an increasing deviation from the standard behavior, due to different tunneling probabilities for spin up and spin down electrons, which causes the spin filtering properties. This model holds qualitatively true until samples with 3 nm barrier. For this value of GdN thickness, which corresponds to a spin filter efficiency of 97%, the curve changes concavity around 4.5 K and becomes convex (see fig. 4.13). Increasing the barrier thickness, the inflection point moves to lower temperatures. In particular,

for 4 nm barrier thick sample, after the first inflection point we observe an incipient increase of I_C at roughly 6 K, which is still to be confirmed by further analysis. IV curves for this sample lose hysteresis at 6 K, hence the critical current has to be determined by means of RSJ fitting [3] (see fig. 4.14).

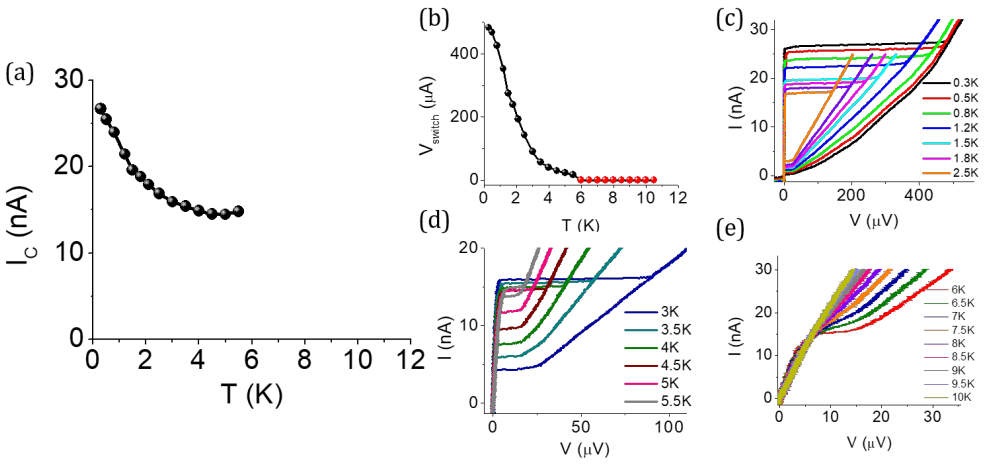

Figure 4.14: (a) $I_C(T)$ up to 5.5 K for spin filter sample with 4 nm thick GdN barrier. (b) Switching voltage. Red points indicate non-hysteretic IV curves. (c) IV curves from 0.3 K to 2.5 K (d) IV curves from 3 K to 5.5 K (e) IV curves from 6 K to 10 K.

In fig. 4.15 we show IV curves for different thicknesses. These measurements highlight how the temperature behavior of the return branch changes with increasing thickness, while for certain temperature ranges depending on the sample, the critical current does not change accordingly. This allows us to exclude that the observed I_C plateau is due to trivial effects of poor thermalization.

Samples with thinner barriers (1.5 nm) show a more conventional behavior, with a subgap branch almost constant at low temperatures. As barrier thickness increase, the subgap branches become almost linear with increasing temperature. In particular, for the thicker sample (fig. 4.15d), the one with a 4 nm barrier, we notice a substantial change in the subgap branches of the IV curves even at low temperatures.

All the previous measurements have been performed at zero field, before applying field, in order to preserve the virgin magnetization state of the barrier. To exclude trivial effects such as flux trapping or accidental magnetization of the barrier, we measured $I_C(H)$ curves at different temperature and collected their maxima. Results are shown in fig. 4.16. As can be seen,

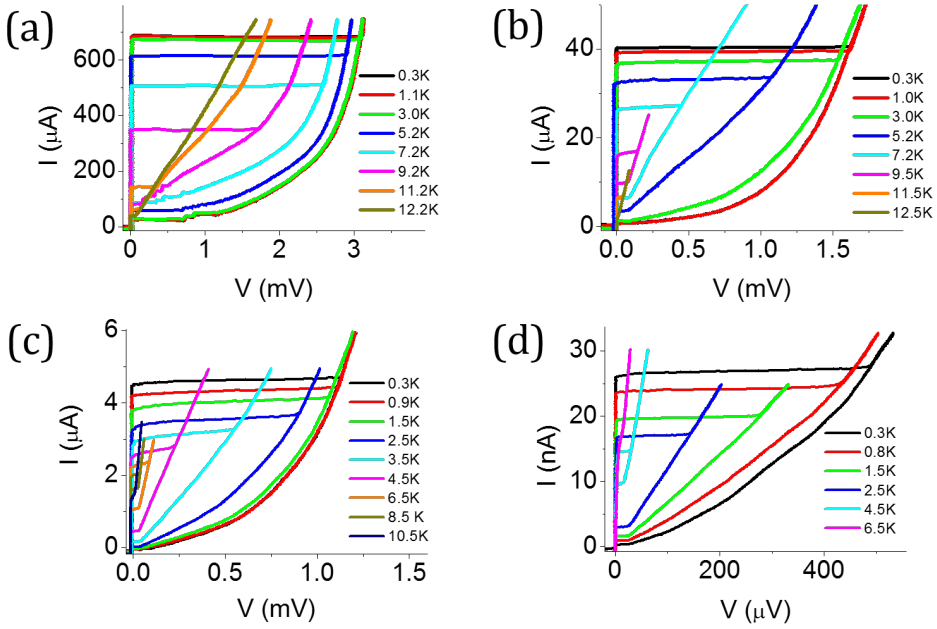

Figure 4.15: IV curves as a function of temperature for different samples with different barrier thicknesses: (a) 1.5 nm, (b) 2.5 nm, (c) 3 nm, (d) 4 nm. The subgap branch remains almost constant at low temperature for samples with thinner barriers, while it changes dramatically with temperature for thicker samples.

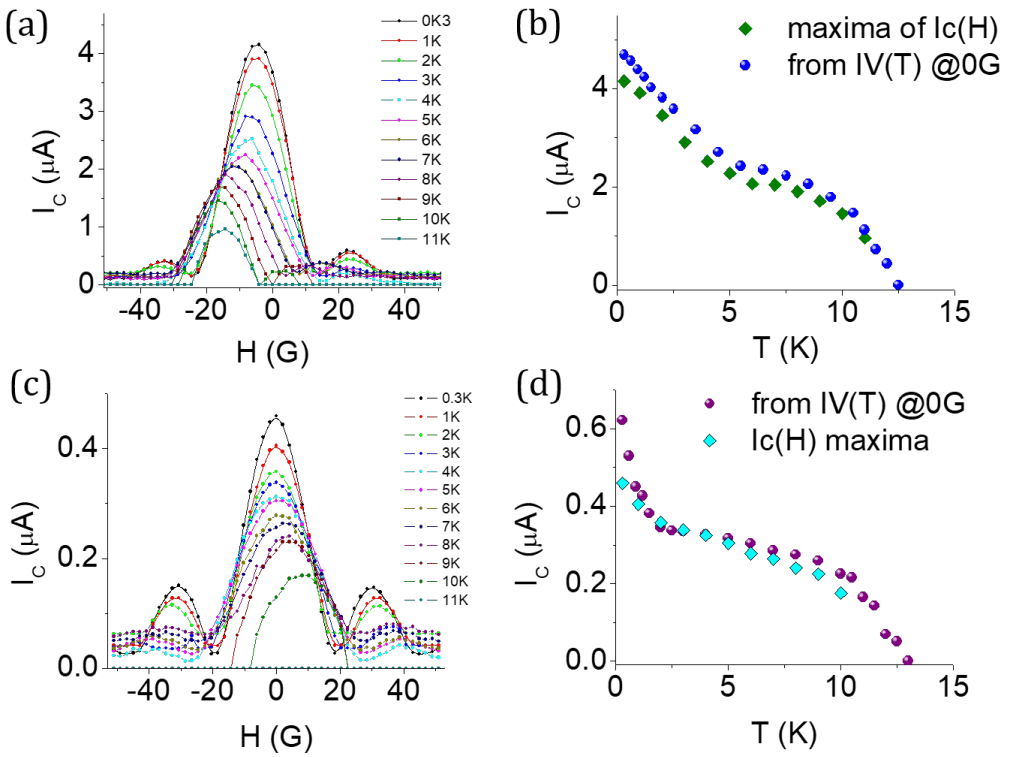

Figure 4.16: (a) Fraunhofer pattern for 3 nm sample. (b) $I_C(T)$ from IV curves (blue dots) and from the maxima of $I_C(H)$ curves (green diamonds). (c) Fraunhofer pattern for 3.5 nm sample. (d) $I_C(T)$ from IV curves (purple dots) and from the maxima of $I_C(H)$ curves (cyan diamonds).

the two curves overlap significantly, so we can exclude trivial effects due to residual or accidental magnetization of the barrier.

One possible preliminary picture that describes the experimental curves refers to works of Bergeret et al. [47] and Eschrig et al. [45], in which the pairing mechanism is described in terms of singlet and triplet Cooper pairs. The anomalous $I_C(T)$ curve is directly related to the presence of a triplet component in the supercurrent, triggered by the exchange field induced in the superconducting electrodes and the spin filtering effect of the barrier. In the model developed in [47], the critical current can be written in terms of singlet and triplet ($S_Z = 0$ and $S_Z = \pm 1$) Green functions, for large enough spin polarization, the singlet component and the triplet component with $S_Z = 0$ are suppressed, and the calculated curves show a good resemblance with our experimental results, suggesting the first direct observation of a triplet supercurrent in spin filter Josephson junctions.

In the work of Tanaka and Kashiwaya [49], the problem is approached using spin-dependent Andreev bound states to describe the effect of a ferromagnetic insulating interface in the clean limit. In this case, the only parameter that describes the spin-dependent energy levels is related to the exchange field in the ferromagnet, and no assumption of spin filtering properties are made. The use of the clean limit constitutes another limit for the applicability of this model to our samples, as with this assumption, in the limit of small exchange field $I_C(T)$ curve assumes the standard form calculated by Kulik and Omelyanchuk [95], instead of the AB dependence expected for tunnel junctions.

4.5.1 Conductance measurements

The experimental data shown to this point suggest the presence of unconventional transport mechanisms giving rise to specific characteristics for spin filter junctions. However, further characterization is necessary to understand which theoretical model is most suitable for the description of such samples. To verify the presence of a single spin active interface as suggested by the second harmonic contribution in $I_C(H)$ curves in sec. 4.4, we measure conductance spectra for different samples, and perform a simple fitting procedure to extrapolate the characteristic parameters of the junctions.

We performed direct measurements of dI/dV as a function of voltage using the setup described in chapter 2. We focused our attention on samples with thickest barrier, namely 3 nm and 4 nm, which show the most pronounced anomalous $I_C(T)$ curve, but we also measured 1.5 nm barrier thick sample, which has a very low spin filter efficiency, and so can be used as term of comparison. Results are shown in fig. 2.4.

Conductance spectra for 1.5 nm sample show a pronounced peak at zero bias at high temperature, while at low temperature the subgap region is flat, except for some structures at $V \sim \Delta$, as for standard tunnel junctions. For thicker samples instead, the subgap region is more rounded, and at high temperature the zero bias peak is still visible.

Fitting

The experimental results of dI/dV curves are qualitatively described using the standard expression for the current in the case of thin samples:

$$I \propto \int_{-\infty}^{+\infty} \rho_1(E)\rho_2(E+V)\,[f(E) - f(E+V)] \tag{4.14}$$

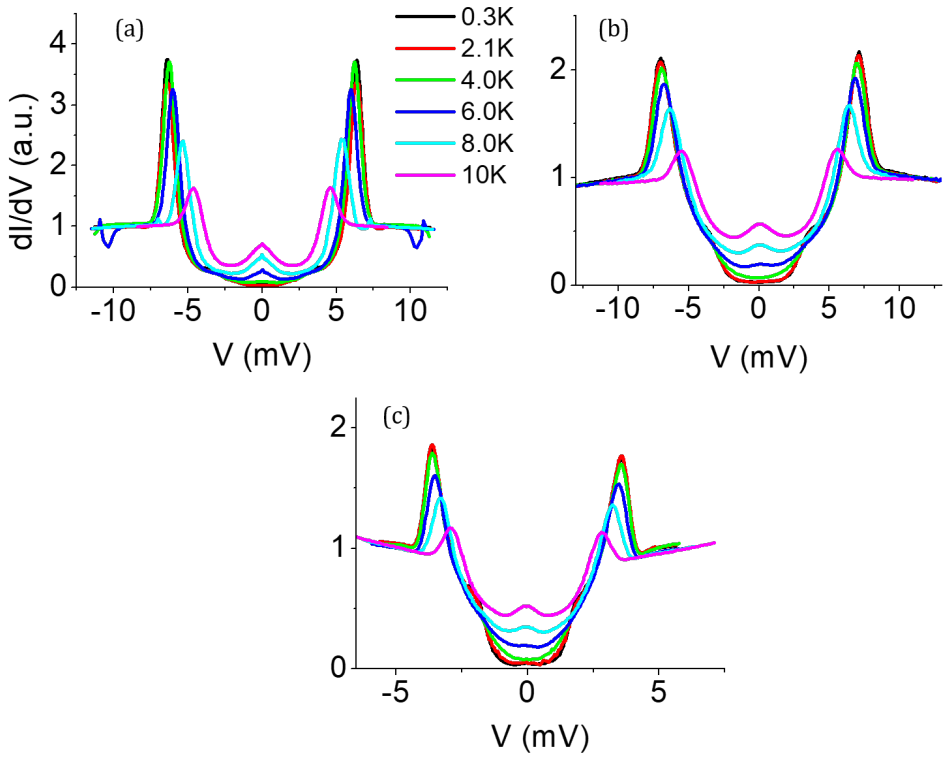

Figure 4.17: Measured dI/dV curves for different samples. (a) 1.5 nm GdN barrier, (b) 3 nm GdN barrier, (c) 4 nm GdN barrier

and using a slightly modified version of the same equation for thicker samples:

$$I \propto a \int_{-\infty}^{+\infty} \rho_1(E+h)\rho_2(E-h+V)\left[f(E)-f(E+V)\right] + b \int_{-\infty}^{+\infty} \rho_1(E-h)\rho_2(E+h+V)\left[f(E)-f(E+V)\right] \tag{4.15}$$

ρ is the density of states, f(E) is the Fermi function, a and b are coefficient used to model spin filter efficiency and h is the exchange field of the ferromagnet. The coefficient a is the spin filter efficiency, estimated from $R(T)$ curves, as explained in 4.2. The exchange field h is estimated from the asymmetry of dI/dV curves. In fact, the positive and negative branch of spin filter samples do not overlap, and the splitting between the two gap peaks can be taken as estimation of the exchange field. The density of states

$$\rho(E) = \frac{1}{c+1}\left(Re\left[\frac{|E-i\Gamma}{\sqrt{(E-i\Gamma)^2-\Delta}}\right]+c\right) \tag{4.16}$$

contains the two fitting parameters used in this work. The parameter Γ is a smearing factor related to the finite lifetime of Cooper pairs [**?**], while c is a finite conductance term.

The fitting curve has been determined minimizing χ^2, defined as

$$\chi^2 = \sum_{i=1}^{N}\left(\frac{G_i-\bar{G}_i}{\sigma}\right)^2 \tag{4.17}$$

over a set of simulated curves obtained for different (Γ, c) pairs, where G_i is the measured value of the conductance dI/dV and $\bar{G}_i$ is the value calculated from simulated curve.

For 1.5 nm sample the fitted curves are in good agreement with experimental data, in particular it is worth to note that the subgap features at low temperatures and the zero bias peak are reproduced by the simulated curves (fig.4.18 a). This agreement confirms the presence of a finite conductance below the gap, and points out the crucial role of smearing, combined with a finite subgap conductance, for the appearance of the subgap structures experimentally observed.

The finite conductance is a strong indication of the presence of different interfaces between the barrier and the superconducting electrodes. Such difference indicates that an appropriate model for spin filter junctions has to include two very different spin active interfaces, or equivalently, a single spin active interface, as predicted in [94] For 3 nm sample, we must include

also $a = 0.97$ and $b = 0.03$, and the exchange energy h due to the ferromagnetic barrier, to take into account the shift with respect to zero voltage. In this case, the agreement between experimental data and fitted curves is still good at low temperatures but becomes poorer at higher temperatures. The application of eq. 4.15 to 4 nm sample gives poor agreement between data and fitted curves also at low temperatures. However, the agreement can be improved at least at low temperatures using different Γ and c in the two electrodes. The spin polarization parameters are fixed to $a = 0.98$ and $b = 0.02$. We assume that in one electrode Γ_1 and c_1 are the ones obtained from the fitting procedure on 1.5 nm sample, while Γ_2 and c_2 in the second electrode are left as fitting parameters. This is a further indication of the presence of a single spin active interface.

The assumption of different parameters in the two electrodes originates from the fact that due to fabrication processes it is likely that the two superconducting electrodes have slightly different properties, and these differences become larger when the barrier thickness increases.

From these results we can infer that a detailed modeling of the transport processes of these junctions has to take into account two very different S/F interfaces, with different properties, which can account for the anomalous CPR and eventually also for the anomalous $I_C(T)$.

However, it is important to stress that the appearance of zero voltage bias peak can be explained only with a combination of a finite conductance below the gap and of a smearing factor. For samples with thicker barrier, and thus high spin filter efficiency, it is possible that this simple model fails to give good predictions because other mechanisms come into play.

4.5.2 Superconducting gap

Conductance spectra also allows the measurement of the superconducting gap of the junctions. To be specific, the conductance peaks correspond to the sum of the superconducting gaps in the two electrodes. In fig. 4.20a we show $\Delta(T)$ for the three samples we measured, namely 1.5 nm, 3 nm and 4 nm. Dashed curves represent BCS fitting of experimental data using[81]

$$\Delta(T) = \Delta(0) \tanh\left(2.2\sqrt{\frac{T - T_C}{T_C}}\right) \tag{4.18}$$

The accuracy of this equation is shown in fig. 4.19, where we compare Δ calculated using standard BCS methods [3], and the approximated function eq. 4.18, with a complete experimental dataset

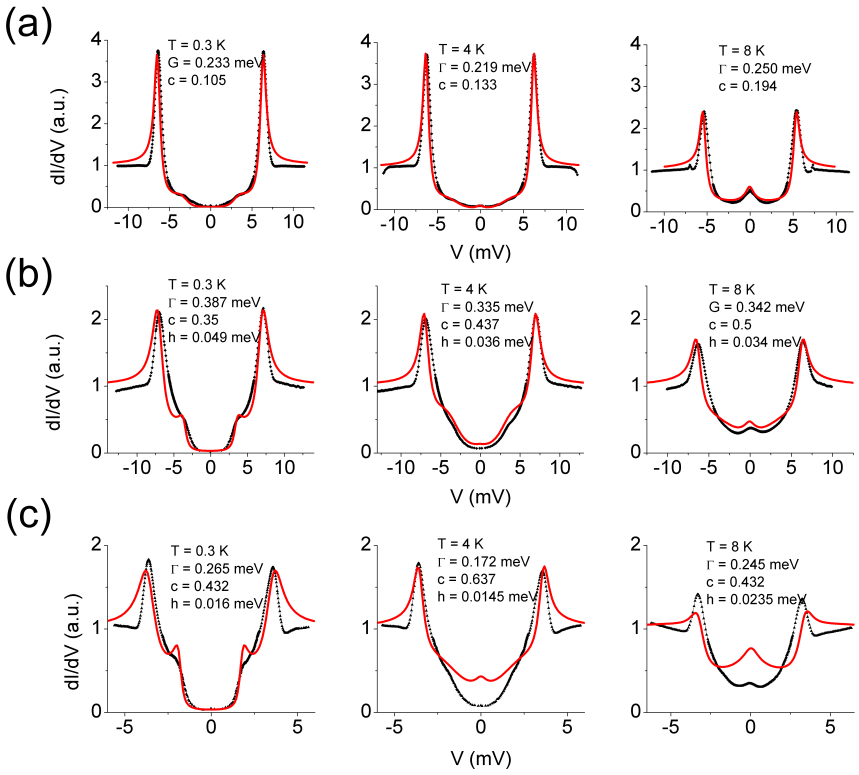

Figure 4.18: Fitting results at different temperatures for (a) 1.5 nm, (b) 3 nm and (c) 4 nm samples

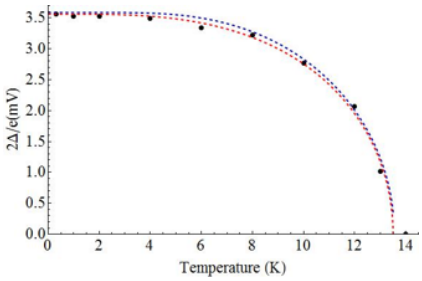

Figure 4.19: Comparison between exerimental data points (black dots), Δ calculated using standard BCS methods[3] (blue dashed line) and Δ approximated by eq. 4.18 (red dashed line).

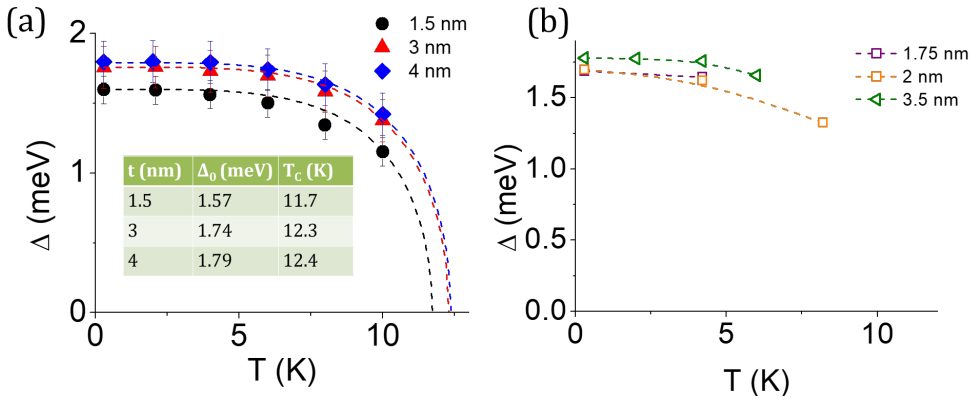

Figure 4.20: (a) $\Delta(T)$ curves obtained from dI/dV measurements for samples with different barrier thicknesses. Red triangles: 3 nm, black dots: 1.5 nm, blue diamonds: 4 nm. Dashed lines: fitted curves. Inset: fitting parameters for each sample. (b) Superconducting gap, calculated by numerically deriving IV curves for junctions with different barrier thickness.

As fitting parameters, we used the zero temperature gap $\Delta(0)$ and the transition temperature T_C. We obtained T_C values compatible with our experimental data from IV curves. The excellent agreement between experimental data and fitted curves guarantee a standard BCS behavior of the superconducting gap, and allows us to exclude gap anomalies as causes of unconventional behavior observed in these junctions.

According to fig. 4.20, the superconducting gap is higher for thicker samples. The lower gap for thinner samples could be due to the fact that for thinner barriers GdN structure is not as smooth as for thicker barriers, and so the NbN counter electrode grows on a worse surface, thus causing a suppression of the superconducting gap.

For samples where dI/dV curves were not measured, we calculated dI/dV numerically to obtain an estimation of the superconducting gap from the position of the conductance peaks. To test our calculation procedure, we compare measured dI/dV and calculated dI/dV for 1.5 nm barrier thick sample. We observe a higher value for Δ estimated from calculated dI/dV, but the discrepancy is not significant as it is within the error bars. What emerges from fig. 4.20b is that the superconducting gap is higher for thicker barriers, which confirms our previous assumption of a worse growth surface in case of thin barriers.

4.6 Phase dynamics and electrodynamical parameters

The transition from thermal activation regime to macroscopic quantum tunneling for NbN/GdN/NbN junctions with high spin filter efficiency has been already demonstrated in previous works [9]. This transition allows the estimation of several electrodynamical parameters of the junction using a self consistent method.

The transition temperature is estimated around 100 mK. Using eq.1.16, and assuming $Q \sim 10$, one can estimate the junction capacitance, which is of the order of a few pF. The switching current distributions in MQT and TA regimes can be fitted using the equations obtained in [96, 8]. The critical current in absence of fluctuations can be estimated from such fitting procedure, and then it can be used to calculate the plasma frequency $\omega_P = \sqrt{\frac{2eI_{C0}}{\hbar C}}$. Using ω_P and C it is possible to give a more refined estimation of the quality factor Q. In the case of the junctions used in this work, the resistance R used in eq. 1.15 is taken equal to the normal state resistance of the junction. For usual tunnel junctions, the resistance that has to be considered for this calculations is the resistance of the environment, which is usually around 100 Ω[7], much smaller than the typical normal state resistances in tunnel junctions. For spin filter junctions instead, the normal state resistance is of the order of 10 Ω for junctions with high spin filter efficiency, and so the assumptions for standard tunnel junctions are no longer valid.

The self consistent estimation of the quality factor for junctions with a critical current $I_C \sim 30\ \mu A$, barrier thickness of 2.5 nm and spin filter efficiency $\sim 90\%$ is Q=10 ± 2[9].

Here we study the switching current distributions for junctions with lower I_C, in order to estimate the junction parameters. For junctions with lower SFE, the high critical current forbid an accurate study of the phase dynamics due to several dissipation processes that come into play[6].

In fig. 4.21 we present SCD measurements on 3 nm barrier sample, with a nominal SFE of $\sim 97\%$. For temperatures between 0.3 K and 3.5 K the junction shows the typical behavior characteristic of thermal activation, withσ increasing as T increases. In particular, $\sigma \propto T^{2/3}$, as observed in a number of experiments investigating standard tunnel junctions in TA regime. For temperatures above 3.5 K, the sharp decrease in σ indicates the transition to PD regime. This transition is confirmed by temperature behavior of the skewness γ. The skewness is defined as as m_3/σ^2, where m_3 is the third central momentum of the statistical distribution, and gives information on the distribution symmetry. Below 3.5 K $\gamma \sim -1$, consistently with switching dis-

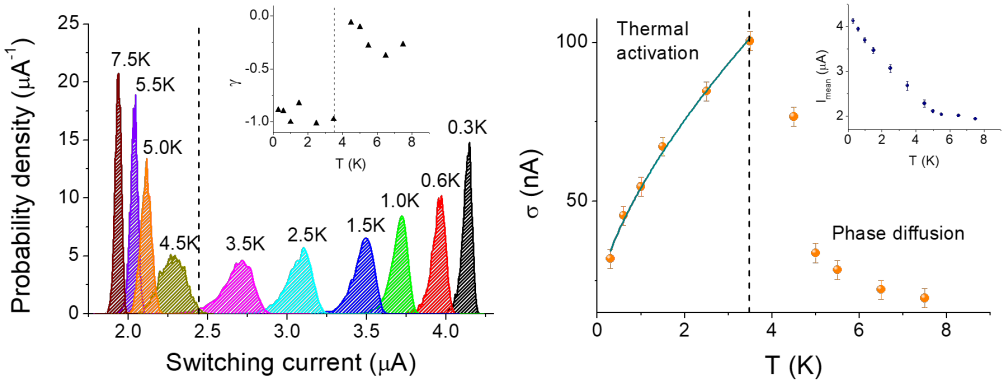

Figure 4.21: Left: switching current distributions at different temperatures for sample with 3 nm barrier. Inset: skewness of the hystograms as a function of temperature. The distributions become more symmetric ($\gamma \sim 0$) in the phase diffusion regime, while they are strongly asymmetric ($\gamma \sim -1$) in the thermal activation regime. Right: distribution width (σ) as a function of temperature for the same sample. Experimental data are in agreement with the expected behavior $T^{2/3}$ up to the transition to PD regime. Inset: mean switching current as a function of temperature. In all figures, black dashed line indicates the transition from TA to PD regime.

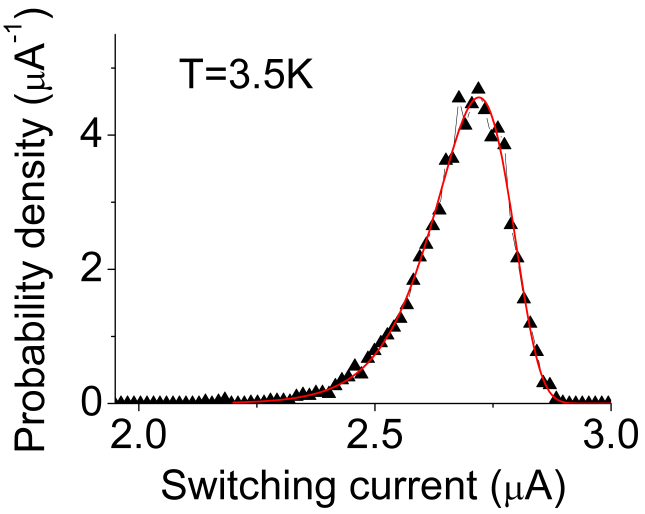

Figure 4.22: Experimental data and fitted curve for switching distribution in thermal activatione regime at 3.5K

tributions in thermal escape regime. Above 3.5 K we observe a progressive symmetrization of the switching current distribution, indicate by γ values close to zero.

From the comparison with samples with higher critical current analyzed elsewhere [9], it is possible to estimate the junction parameters. From the capacitance C estimated previously, we estimate the permittivity of GdN to be $2.7 \pm 0.5 F/m$. This allows us to calculate an approximate value for C for other samples. In particular, for 3 nm barrier sample we obtain $C = 4.4 \pm 0.9 pF$. We can now calculate the quality factor for this junction. Using 1.15 we obtain $Q = 5 \pm 1.5$. This value is in agreement with the experimental observation of phase diffusion in switching dynamics, which is known to occur in moderately damped ($1<Q<5$) systems.

In fig. 4.23 we show SCD measurements for the sample with barrier thickness of 3.5 nm. In this case, the current distributions have the typical behavior of phase diffusion regime in the whole temperature range, with $\sigma(T)$ curve, which is decreasing in the whole temperature range. Applying the same procedure explained previously, we obtain $C = 3.8 \pm 0.8 pF$, which leads to a quality factor $Q = 2.6 \pm 0.8$. As expected, this value is lower than the one obtained for 3 nm barrier thick sample, and in agreement with a lower transition temperature from TA to PD.

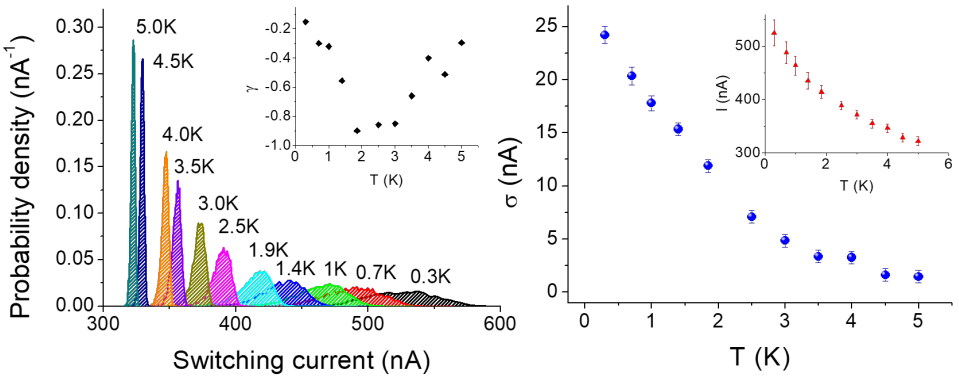

Figure 4.23: Left: switching current distributions at different temperatures for sample with 3.5 nm barrier. Inset: skewness of the hystograms as a function of temperature. Right: distribution width (σ) as a function of temperature for the same sample. The negative derivative of σ in the whole temperature range indicates that the system is in PD regime. Inset: mean switching current as a function of temperature.

Conclusions

We have fully characterized the properties of two different types of ferromagnetic junctions, namely SIsFS junctions and SI$_F$S junctions. Both these junctions are underdamped and characterized by relatively high $I_C R_N$ values. They definitely fall in the category of promising ferromagnetic devices, with potential for future developments in superconducting electronics, including components of quantum hybrid circuits.

We demonstrated the possible use of microwaves fields as an additional knob to manipulate the memory state of MJJs with a Al/AlO$_x$-Nb-PdFe barrier. In particular, we have shown how the application of an external RF signal combined with a magnetic field pulse can enhance the switching between logical states.

We characterized the effect as a function of different parameters, namely temperature, field pulse amplitude and nominal energy of the RF train. We have identified the optimal operational range for the use of microwaves on SIsFS samples with PdFe barrier. The ferromagnetic properties of PdFe are due to two different magnetization mechanisms, characterized by two different Curie temperatures. For this reason, the optimal working temperature for PdFe-based devices is close to the lower Curie temperature of the ferromagnet. In this temperature range, RF signal is capable of switching off one of the two mechanisms, thus facilitating the remagnetization of the barrier.

The use of RF fields to address magnetic memories compatible with SFQ logic is a possible alternative solution towards energy-efficient components for hybrid quantum architectures, and to develop a new class of addressing schemes using only RF fields in low-dissipation magnetic memories.

We also performed a complete low-temperature characterization of low dissipation spin filter junctions, with barrier thicknesses ranging from 1.5 nm to 4 nm. In virtue of future applications in superconducting spintronics and quantum circuits, a full characterization of the phase dynamics of such junctions using SCDs is needed, and also a reliable estimation of the junction parameters such as the capacitance and the quality factor.

Our outcomes allow to give a consistent picture of the phase dynamics of

these junctions, pointing out anomalous behaviors which might be consistent with long range triplet correlations. In particular, we observed an anomalous $I_C(T)$ dependence, supported by $I_C(H)$ measurements as a function of temperature. The remarkable feature of these samples is the progressive growth of the anomalous features when increasing the barrier thickness, and thus the expected triplet contribution. For thicker barriers, $I_C(T)$ curves show a plateau at intermediate temperatures, followed by a linear increase at low temperatures consistent with theoretical models of spin triplet superconductivity.

We believe that in virtue of their properties spin filter junctions could be an extremely flexible tool for future developments in superconducting spintronics and other high performance computational approaches. We envisage the possibility of using ferromagnetic junctions with low dissipation in transmon qubits. In low dissipation ferromagnetic junctions, the Josephson energy can be changed by driving critical current levels with low noise RF fields, as demonstrated in this work.

Bibliography

[1] B. D. Josephson, "Possible new effects in superconductive tunnelling," *Phys. Lett.*, vol. 1, pp. 251 – 253, 1962.

[2] A. A. Golubov, M. Y. Kupriyanov, and E. Ilćhev, "The current-phase relation in Josephson junctions," *Rev. Mod. Phys.*, vol. 76, p. 411, 2004.

[3] A. Barone and G. Paterno, *Physics and Applications of the Josephson effect*. John Wiley & sons, 1982.

[4] K. K. Likharev, *Dynamics of Josephson junctions and circuits*. Gordon and Breach Science Publishers, 1986.

[5] S. Shapiro, "Josephson currents in superconducting tunneling: The effect of microwaves and other observations," *Phys. Rev. Lett.*, vol. 11, pp. 80–82, Jul 1963.

[6] M. H. Devoret, J. M. Martinis, and J. Clarke, "Measurements of macroscopic quantum tunneling out of the zero-voltage state of a current-biased Josephson junction," *Phys. Rev. Lett.*, vol. 55, p. 1908, 1985.

[7] J. M. Martinis and R. L. Kautz, "Classical phase diffusion in small hysteretic Josephson junctions," *Phys. Rev. Lett.*, vol. 63, pp. 1507–1510, Oct 1989.

[8] A. O. Caldeira and A. J. Leggett, "Influence of dissipation on quantum tunneling in macroscopic systems," *Phys. Rev. Lett.*, vol. 46, p. 211, 1981.

[9] D. Massarotti, A. Pal, G. Rotoli, L. Longobardi, M. G. Blamire, and F. Tafuri, "Macroscopic quantum tunnelling in spin filter ferromagnetic Josephson junctions," *Nat. Comm.*, vol. 6, p. 7376, 2015.

[10] L. Longobardi, D. Massarotti, D. Stornaiuolo, L. Galletti, G. Rotoli, F. Lombardi, and F. Tafuri, "Direct transition from quantum escape to

a phase diffusion regime in YBaCuO biepitaxial Josephson junctions," *Phys. Rev. Lett.*, vol. 109, p. 050601, Aug 2012.

[11] D. Massarotti, D. Stornaiuolo, P. Lucignano, L. Galletti, D. Born, G. Rotoli, F. Lombardi, L. Longobardi, A. Tagliacozzo, and F. Tafuri, "Breakdown of the escape dynamics in Josephson junctions," *Phys. Rev. B*, vol. 92, p. 054501, Aug 2015.

[12] H. Grabert, P. Olschowski, and U. Weiss, "Quantum decay rates for dissipative systems at finite temperatures," *Phys. Rev. B*, vol. 36, p. 1931, 1987.

[13] M. Iansiti, M. Tinkham, A. T. Johnson, W. F. Smith, and C. J. Lobb, "Charging effects and quantum properties of small superconducting tunnel junctions," *Phys. Rev. B*, vol. 39, pp. 6465–6484, Apr 1989.

[14] J. Männik, S. Li, W. Qiu, W. Chen, V. Patel, S. Han, and J. E. Lukens, "Crossover from kramers to phase-diffusion switching in moderately damped Josephson junctions," *Phys. Rev. B*, vol. 71, p. 220509, Jun 2005.

[15] J. M. Kivioja, T. E. Nieminen, J. Claudon, O. Buisson, F. W. J. Hekking, and J. P. Pekola, "Observation of transition from escape dynamics to underdamped phase diffusion in a Josephson junction," *Phys. Rev. Lett.*, vol. 94, p. 247002, Jun 2005.

[16] V. M. Krasnov, T. Golod, T. Bauch, and P. Delsing, "Anticorrelation between temperature and fluctuations of the switching current in moderately damped Josephson junctions," *Phys. Rev. B*, vol. 76, p. 224517, Dec 2007.

[17] M.-H. Bae, M. Sahu, H.-J. Lee, and A. Bezryadin, "Multiple-retrapping processes in the phase-diffusion regime of high-T_c intrinsic Josephson junctions," *Phys. Rev. B*, vol. 79, p. 104509, Mar 2009.

[18] H. F. Yu, X. B. Zhu, Z. H. Peng, Y. Tian, D. J. Cui, G. H. Chen, D. N. Zheng, X. N. Jing, L. Lu, S. P. Zhao, and S. Han, "Quantum phase diffusion in a small underdamped Josephson junction," *Phys. Rev. Lett.*, vol. 107, p. 067004, Aug 2011.

[19] D. Halliday, R. Resnick, J. Walker, F. Edwards, and J. J. Merrill, *Fundamental of Physics.* John Wiley & Sons, Inc., 10 ed., 2013.

[20] K. K. Likharev, "Superconducting weak links," *Rev. Mod. Phys*, vol. 51, p. 102, 1979.

[21] A. I. Buzdin, "Proximity effects in superconductor-ferromagnet heterostructures," *Rev. Mod. Phys.*, vol. 77, pp. 935–976, 2005.

[22] V. L. Ginzburg and L. D. Landau *Zh. Eksperim. i Theor. Fiz.*, vol. 20, p. 1064, 1950.

[23] J. Bardeen, L. N. Cooper, and J. R. Schrieffer, "Theory of superconductivity," *Phys. Rev.*, vol. 108, pp. 1175–1204, 1957.

[24] F. S. Bergeret, A. F. Volkov, and K. B. Efetov, "Odd triplet superconductivity and related phenomena in superconductor-ferromagnet structures," *Rev. Mod. Phys.*, vol. 77, pp. 1321–1373, Nov 2005.

[25] A. Larkin and Y. Ovchinnikov, "Inhomogeneous state of superconductors," *Sov. Phys. JETP*, vol. 20, p. 762, 1964.

[26] P. Fulde and R. Ferrell, "Superconductivity in a strong spin-exchange field," *Phys. Rev.*, vol. 135, p. A550, 1964.

[27] G. Eilenberger, "Transformation of Gorkov's equation for type II superconductors into transport-like equations," *Z. Phys.*, vol. 214, p. 195, 1968.

[28] L. Usadel, "Generalized diffusion equation for superconducting alloys," *Phys. Rev. Lett.*, vol. 81, p. 3247, 1970.

[29] L. N. Bulaevskii, V. V. Kuzii, and A. A. Sobyanin, "Superconducting system with weak coupling to the current in the ground state," *JETP Lett.*, vol. 25, p. 290, 1977.

[30] T. Kontos, M. Aprili, J. Lesueur, and X. Grison, "Inhomogeneous superconductivity induced in a ferromagnet by proximity effect," *Phys. Rev. Lett.*, vol. 86, pp. 304–307, Jan 2001.

[31] T. Kontos, M. Aprili, J. Lesueur, F. Genêt, B. Stephanidis, and R. Boursier, "Josephson junction through a thin ferromagnetic layer: Negative coupling," *Phys. Rev. Lett.*, vol. 89, p. 137007, Sep 2002.

[32] V. V. Ryazanov, V. A. Oboznov, A. Y. Rusanov, A. V. Veretennikov, A. A. Golubov, and J. Aarts, "Coupling of two superconductors through a ferromagnet: Evidence for a π junction," *Phys. Rev. Lett.*, vol. 86, pp. 2427–2430, Mar 2001.

[33] Y. Blum, A. Tsukernik, M. Karpovski, and A. Palevski, "Oscillations of the superconducting critical current in Nb-Cu-Ni-Cu-Nb junctions," *Phys. Rev. Lett.*, vol. 89, p. 187004, Oct 2002.

[34] A. Bauer, J. Bentner, M. Aprili, M. L. Della Rocca, M. Reinwald, W. Wegscheider, and C. Strunk, "Spontaneous supercurrent induced by ferromagnetic π junctions," *Phys. Rev. Lett.*, vol. 92, p. 217001, May 2004.

[35] H. Sellier, C. Baraduc, F. m. c. Lefloch, and R. Calemczuk, "Half-integer shapiro steps at the $0-\pi$ crossover of a ferromagnetic Josephson junction," *Phys. Rev. Lett.*, vol. 92, p. 257005, Jun 2004.

[36] E. Goldobin, D. Koelle, R. Kleiner, and A. Buzdin, "Josephson junctions with second harmonic in the current-phase relation: Properties of φ junctions," *Phys. Rev. B*, vol. 76, p. 224523, Dec 2007.

[37] H. Sickinger, A. Lipman, M. Weides, R. G. Mints, H. Kohlstedt, D. Koelle, R. Kleiner, and E. Goldobin, "Experimental evidence of a φ Josephson junction," *Phys. Rev. Lett.*, vol. 109, p. 107002, Sep 2012.

[38] R. S. Keizer, S. T. B. Goennenwein, T. M. Klapwijk, G. Miao, G. Xiao, and A. Gupta, "A spin triplet supercurrent through the half-metallic ferromagnet CrO_2," *Nature*, vol. 439, p. 825, 2006.

[39] T. S. Khaire, M. A. Khasawneh, W. P. Pratt, and N. O. Birge, "Observation of spin-triplet superconductivity in Co-based Josephson junctions," *Phys. Rev. Lett.*, vol. 104, p. 137002, Mar 2010.

[40] J. W. A. Robinson, J. Witt, and M. Blamire, "Controlled injection of spin-triplet supercurrents into a strong ferromagnet," *Science*, vol. 329, p. 59, 2010.

[41] C. Klose, T. S. Khaire, Y. Wang, W. P. Pratt, N. O. Birge, B. J. McMorran, T. P. Ginley, J. A. Borchers, B. J. Kirby, B. B. Maranville, and J. Unguris, "Optimization of spin-triplet supercurrent in ferromagnetic Josephson junctions," *Phys. Rev. Lett.*, vol. 108, p. 127002, Mar 2012.

[42] A. Di Bernardo, S. Diesch, Y. Gu, J. Linder, G. Divitini, C. Ducati, E. Scheer, M. G. Blamire, and J. W. A. Robinson, "Signature of magnetic-dependent gapless odd frequency states at superconductor/ferromagnet interfaces," *Nat. Comm.*, vol. 6, p. 8053, 2015.

[43] M. Anwar, M. Veldhorst, A. Brinkman, and J. Aart, "Long range supercurrents in ferromagnetic $Cr0_2$ using a multilayer contact structure," *Appl. Phys. Lett*, vol. 100, p. 052602, 2012.

[44] P. V. Leksin, N. N. Garif'yanov, I. A. Garifullin, Y. V. Fominov, J. Schumann, Y. Krupskaya, V. Kataev, O. G. Schmidt, and B. Büchner, "Evidence for triplet superconductivity in a superconductor-ferromagnet spin valve," *Phys. Rev. Lett.*, vol. 109, p. 057005, Aug 2012.

[45] M. Eschrig and T. Löfwander, "Triplet supercurrents in clean and disordered half-metallic ferromagnets," *Nat. Phys.*, vol. 4, p. 138, 2008.

[46] F. S. Bergeret, A. F. Volkov, and K. B. Efetov, "Josephson current in superconductor-ferromagnet structures with a nonhomogeneous magnetization," *Phys. Rev. B*, vol. 64, p. 134506, Sep 2001.

[47] F. S. Bergeret, A. Verso, and A. F. Volkov, "Spin-polarized Josephson and quasiparticle currents in superconducting spin-filter tunnel junctions," *Phys. Rev. B*, vol. 86, p. 060506, 2012.

[48] S. Kawabata, Y. Asano, Y. Tanaka, A. A. Golubov, and S. Kashiwaya, "Josephson π state in a ferromagnetic insulator," *Phys. Rev. Lett.*, vol. 104, p. 117002, Mar 2010.

[49] Y. Tanaka and S. Kashiwaya, "Theory of Josephson effect in superconductor-ferromagnetic-insulator-superconductor junction," *Physica C: Superconductivity*, vol. 274, no. 3, pp. 357 – 363, 1997.

[50] V. Bol'ginov, V. Stolyarov, D. Sobanin, A. Karpovich, and V. Ryazanov *JETP Lett.*, vol. 95, p. 366, 2012.

[51] L. Longobardi, D. Massarotti, G. Rotoli, D. Stornaiuolo, G. Papari, A. Kawakami, G. P. Pepe, A. Barone, and F. Tafuri, "Thermal hopping and retrapping of a brownian particle in the tilted periodic potential of a NbN/MgO/NbN Josephson junction," *Phys. Rev. B*, vol. 84, p. 184504, 2011.

[52] L. Longobardi, D. Massarotti, G. Rotoli, D. Stornaiuolo, G. Papari, A. Kawakami, G. P. Pepe, A. Barone, and F. Tafuri, "Quantum crossover in moderately damped epitaxial nbn/mgo/nbn junctions with low critical current density," *Appl. Phys. Lett.*, vol. 99, p. 062510, 2011.

[53] M. Tinkham, *Introduction to superconductivity.* Dover publications, 2 ed., 2002.

[54] D. S. Holmes, A. L. Ripple, and M. A. Manheimer, "Energy-efficient superconducting computing—power budgets and requirements," *IEEE Trans. Appl. Supercond.*, vol. 23, p. 1701610, 2013.

[55] T. V. Duzer, L. Zheng, S. R. Whiteley, H. Kim, J. Kim, X. Meng, and T. Ortlepp *IEEE Trans. Appl. Supercond.*, vol. 23, p. 1700504, 2013.

[56] L. Ye, D. B. Gopman, L. Rehm, D. Backes, G. Wolf, T. Ohki, A. Kirichenko, I. Vernik, O. Mukhanov, and A. Kent *J. Appl. Phys.*, vol. 115, p. 17C725, 2014.

[57] S. V. Aradhya, G. E. Rowlands, J. Oh, D. C. Ralph, and R. A. Burman *Nano Lett.*, vol. 16, p. 5987, 2016.

[58] B. Baek, W. H. Rippard, S. P. Benz, S. E. Russek, and P. D. Dresselhaus *Nat. Commun.*, vol. 5, p. 4888, 2014.

[59] M. A. E. Qader, R. K. Singh, S. N. Galvin, L. Yu, J. Rowell, and N. Newman *Appl. Phys. Lett.*, vol. 104, p. 022602, 2014.

[60] B. M. Niedzielski, E. C. Gingrich, R. Loloee, W. Pratt, and N. Birge *Supercond. Sci. Technol.*, vol. 28, p. 085012, 2015.

[61] T. Larkin, V. Bol'ginov, V. Stolyarov, V. Ryazanov, I. Vernik, S. Tolpygo, and O. Mukhanov *Appl. Phys. Lett.*, vol. 100, p. 222601, 2012.

[62] I. V. Vernik, V. V. Bol'ginov, S. V. Bakurskiy, A. Golubov, M. Y. Kupriyanov, V. Ryazanov, and O. Mukhanov *IEEE Trans. Appl. Supercond.*, vol. 23, p. 1701208, 2013.

[63] E. C. Gingrich, B. M. Niedzielski, J. A. Glick, Y. Wang, D. L. Miller, R. Loloee, W. P. Pratt, and N. O. Birge, "Controllable $0-\pi$ josephson junctions containing a ferromagnetic spin valve," *Nat. Physics*, vol. 12, pp. 564 – 567, 2016.

[64] I. M. Dayton, T. Sage, E. C. Gingrich, M. G. Loving, T. F. Ambrose, N. P. Siwak, S. Keebaugh, C. Kirby, D. L. Miller, A. Y. Herr, Q. P. Herr, and O. Naaman, "Experimental demonstration of a josephson magnetic memory cell with a programmable π-junction," *arXiv*, no. 1711.01681, 2017.

[65] C. Thirion, W. Wernsdorfer, and D. Mailly, "Switching of magnetization by nonlinear resonance studied in single nanoparticles," *Nat. Materials*, vol. 2, p. 524, 2003.

[66] T. Moriyama, R. Cao, J. Q. Xiao, X. R. Wang, Q. Wen, and H. W. Zhang *Appl. Phys. Lett.*, vol. 90, p. 152503, 2007.

[67] C. Raufast, A. Tamion, E. Bernstein, V. Dupuis, T. Tournier, T. Crozes, E. Bonet, and W. Wernsdorfer *IEEE Trans. Magn.*, vol. 44, p. 2812, 2008.

[68] X. Fan, Y. S. Gui, A. Wirthmann, G. Williams, D. Xue, and C.-M. Hu *Appl. Phys. Lett.*, vol. 95, p. 062511, 2009.

[69] S. Okamoto, N. Kikuchi, O. Kitakami, T. Shimatsu, and H. Aoi *J. Appl. Phys.*, vol. 109, p. 07B748, 2011.

[70] L. Cai, D. A. Garanin, and E. M. Chudnovsky *Phys. Rev. B*, vol. 87, p. 024418, 2013.

[71] H. Suto, T. Kanao, T. Nagasawa, K. Kudo, K. Mizushima, and R. Sato *Appl. Phys. Lett.*, vol. 110, p. 262403, 2017.

[72] I. A. Golovchanskiy, V. V. Bolginov, N. N. Abramov, V. S. Stolyarov, A. Ben Hamida, V. I. Chichkov, D. Roditchev, and V. V. Ryazanov *J. Appl. Phys.*, vol. 120, p. 163902, 2016.

[73] S. J. Greaves, H. Muraoka, and Y. Kanai, "Optimisation of applied field pulses for microwave assisted magnetic recording," *AIP Advances*, vol. 7, no. 5, p. 056517, 2017.

[74] D. Yohannes, S. Sarwana, S. Tolpygo, A. Sahu, and V. Semenov *IEEE Trans. Appl. Supercond.*, vol. 15, p. 90, 2015.

[75] S. Tolpygo, D. Yohannes, R. Hunt, J. Vuvalda, D. Donnelly, D. Amparo, and A. Kirichenko *IEEE Trans. Appl. Supercond*, vol. 17, p. 946, 2007.

[76] S. Bakurskiy, N. Klenov, I. Soloviev, V. Bol'ginov, V. Ryazanov, I. Vernik, O. Mukhanov, M. Kupriyanov, and A. Golubov *Appl. Phys. Lett.*, vol. 102, p. 192603, 2013.

[77] A. S. Vasenko, A. A. Golubov, M. Y. Kupriyanov, and M. Weides, "Properties of tunnel Josephson junctions with a ferromagnetic interlayer," *Phys. Rev. B*, vol. 77, p. 134507, Apr 2008.

[78] H. H. Zappe, "Minimum current and related topics in Josephson tunnel junction devices," *J. Appl. Phys.*, vol. 44, p. 1371, 1973.

[79] V. Bol'ginov, O. Tikhomirov, and L. Uspenskaya *JETP Lett.*, vol. 105, p. 169, 2017.

[80] A. Pal, Z. Barber, J. Robinson, and M. Blamire, "Pure second harmonic current-phase relation in spin-filter Josephson junctions," *Nat. Comm.*, vol. 5, p. 3340, 2014.

[81] K. Senapati, M. G. Blamire, and Z. H. Barber, "Spin-filter Josephson junctions," *Nature Materials*, vol. 10, p. 849, 2011.

[82] K. Senapati, T. Fix, M. E. Vickers, M. G. Blamire, and Z. H. Barber, "Structural evolution and competing magnetic orders in polycrystalline GdN films," *Phys. Rev. B*, vol. 83, p. 014403, Jan 2011.

[83] J. G. Simmons, "Generalized formula for the electric tunnel effect between similar electrodes separated by a thin insulating film," *J. Appl. Phys.*, vol. 34, p. 1793, 1963.

[84] G. Grosso and G. Pastore Parravicini, *Solid State Physics*. Academic press, 2003.

[85] Y. M. Blanter and F. W. J. Hekking, "Supercurrent in long SFFS junctions with antiparallel domain configuration," *Phys. Rev. B*, vol. 69, p. 024525, Jan 2004.

[86] A. Vedyayev, C. Lacroix, N. Pugach, and N. Ryzhanova, "Spin-valve magnetic sandwich in a Josephson junction," *EPL (Europhysics Letters)*, vol. 71, no. 4, p. 679, 2005.

[87] B. Crouzy, S. Tollis, and D. A. Ivanov, "Josephson current in a superconductor-ferromagnet junction with two noncollinear magnetic domains," *Phys. Rev. B*, vol. 75, p. 054503, Feb 2007.

[88] O. Kashuba, Y. M. Blanter, and V. I. Fal'ko, "$0-\pi$ transition in superconductor-ferromagnet-superconductor junctions with strongly spin-dependent scattering," *Phys. Rev. B*, vol. 75, p. 132502, Apr 2007.

[89] F. S. Bergeret, A. F. Volkov, and K. B. Efetov, "Josephson current in superconductor-ferromagnet structures with a nonhomogeneous magnetization," *Phys. Rev. B*, vol. 64, p. 134506, Sep 2001.

[90] M. A. Khasawneh, W. P. Pratt, and N. O. Birge, "Josephson junctions with a synthetic antiferromagnetic interlayer," *Phys. Rev. B*, vol. 80, p. 020506, Jul 2009.

[91] B. M. Ludbrook, I. L. Farrell, M. Kuebel, B. J. Ruck, A. R. H. Preston, H. J. Trodahl, L. Ranno, R. J. Reeves, and S. M. Durbin, "Growth and properties of epitaxial GdN," *J. Appl. Phys.*, vol. 106, p. 063910, 2009.

[92] W. C. Stewart *Appl. Phys. Lett.*, vol. 12, p. 277, 1968.

[93] W. C. Stewart *J. Appl. Phys.*, vol. 45, p. 452, 1974.

[94] L. Trifunovic, "Long-range superharmonic Josephson current," *Phys. Rev. Lett.*, vol. 107, p. 047001, Jul 2011.

[95] I. O. Kulik and A. N. Omelyanchuk *Sov. J. Low Temp. Phys.*, vol. 3, p. 459, 1977.

[96] H. A. Kramers, "Brownian motion in a field of force and the diffusion model of chemical reactions," *Physica*, p. 284, 1940.